

# Computer-assisted proof of heteroclinic connections in the one-dimensional Ohta-Kawasaki model

Jacek Cyranka<sup>\*,‡,†</sup>, Thomas Wanner<sup>§</sup>

<sup>‡</sup> Institute of Computer Science and Computational Mathematics, Jagiellonian University  
ul. S. Łojasiewicza 6, 30-348 Kraków, Poland

<sup>†</sup> Institute of Applied Mathematics and Mechanics, University of Warsaw  
Banacha 2, 02-097 Warszawa, Poland

<sup>\*</sup> Department of Mathematics, Rutgers, The State University of New Jersey, 110 Frelinghusen Rd, Piscataway,  
NJ 08854-8019, USA

<sup>§</sup> Department of Mathematical Sciences, George Mason University, Fairfax, VA 22030, USA

jcyranka@gmail.com, jacek.cyranka@ii.uj.edu.pl, twanner@gmu.edu

October 11, 2024

**Abstract.** We present a computer-assisted proof of heteroclinic connections in the one-dimensional Ohta-Kawasaki model of diblock copolymers. The model is a fourth-order parabolic partial differential equation subject to homogeneous Neumann boundary conditions, which contains as a special case the celebrated Cahn-Hilliard equation. While the attractor structure of the latter model is completely understood for one-dimensional domains, the diblock copolymer extension exhibits considerably richer long-term dynamical behavior, which includes a high level of multistability. In this paper, we establish the existence of certain heteroclinic connections between the homogeneous equilibrium state, which represents a perfect copolymer mixture, and all local and global energy minimizers. In this way, we show that not every solution originating near the homogeneous state will converge to the global energy minimizer, but rather is trapped by a stable state with higher energy. This phenomenon can not be observed in the one-dimensional Cahn-Hilliard equation, where generic solutions are attracted by a global minimizer.

The proof of the above statement is conceptually simple, and combines several techniques from some of the authors' and Zgliczyński's works. Central for the verification is the rigorous propagation of a piece of the unstable manifold of the homogeneous state with respect to time. This propagation has to lead to small interval bounds, while at the same time entering the basin of attraction of the stable fixed point. For interesting parameter values the global attractor exhibits a complicated equilibrium structure, and the dynamical equation is rather stiff. This leads to a time-consuming numerical propagation of error bounds, with many integration steps. This problem is addressed using an efficient algorithm for the rigorous integration of partial differential equations forward in time. The method is able to handle large integration times within a reasonable computational time frame, and this makes it possible to establish heteroclinic at various nontrivial parameter values.

**Keywords:** Diblock copolymer model, dissipative partial differential equation, attractor structure, heteroclinic connection, multistability, computer-assisted proof.

**AMS classification:** Primary: 35B40, 35B41, 35K55, 65C20. Secondary: 35Q99, 15B99, 68U20.

# 1 Introduction

Phase separation phenomena in materials sciences provide a rich source for pattern formation mechanisms. In many situations, the resulting models are dissipative parabolic partial differential equations which are amenable to rigorous mathematical treatment, and can therefore explain the underlying pattern formation principles. In the current paper, we consider one of these models which has been of significant interest in recent years. This equation is of phase field type, and it models microphase separation in diblock copolymers. From a mathematical perspective, the model has been described in [37], in its original form it was proposed by Ohta and Kawasaki [38], as well as Bahiana and Oono [1]. See also the discussion in [9, 10]. If one considers a material constrained to the bounded domain  $\Omega \subset \mathbb{R}^d$ , then the diblock copolymer model considers a free-energy functional for the relative macroscopic monomer concentration  $u$ , i.e., for the difference between the two monomer volume fractions, given by

$$E_{\epsilon,\sigma}[u] = \int_{\Omega} \left( \frac{\epsilon^2}{2} |\nabla u|^2 + F(u) \right) dx + \frac{\sigma}{2} \int_{\Omega} |(-\Delta)^{-1/2}(u(x) - \mu)|^2 dx . \quad (1)$$

In this energy, the real number  $\mu = \int_{\Omega} u dx / |\Omega|$  denotes the average mass of  $u$ , and the nonlinear function  $F$  is a double-well potential with global minima at  $\pm 1$ . For the purposes of this paper, we consider the standard double-well potential  $F(u) = (u^2 - 1)^2/4$ . Note that the energy functional (1) is just the standard van der Waals free energy, but with an additional nonlocal term which integrates the square root of the inverse Laplacian on a space of functions with zero total mass. With the energy functional  $E_{\epsilon,\sigma}[u]$  one can associate gradient-like dynamics, which is then used to model the evolution of the material as a function of time. While this can be accomplished in a variety of ways, the diblock copolymer model in its standard form considers the evolution equation

$$\begin{aligned} u_t &= -\Delta \left( \epsilon^2 \Delta u + f(u) \right) - \sigma(u - \mu) \quad \text{in } \Omega , \\ \mu &= \frac{1}{|\Omega|} \int_{\Omega} u(x) dx , \quad \text{and} \quad \frac{\partial u}{\partial \nu} = \frac{\partial \Delta u}{\partial \nu} = 0 \quad \text{on } \partial\Omega , \end{aligned} \quad (2)$$

where the nonlinearity is defined as  $f(u) = -F'(u)$ , and which in our situation is given by  $f(u) = u - u^3$ . This evolution equation is based on the gradient in the  $H^{-1}$ -topology and uses homogeneous Neumann boundary conditions for both  $u$  and  $\Delta u$ .

The evolution equation (2) describes the evolution of a diblock copolymer in the following way. The value of the phase variable  $u$  describes the local material composition through the convention that values of  $u(t, x)$  which are close to  $+1$  are interpreted as only monomer A being present at a material point  $x \in \Omega$  and at time  $t \geq 0$ , while the value  $-1$  indicates that only monomer B is present. Mixtures of the two monomers are indicated by  $u$ -values in between, and the value zero corresponds to an equal mixture of the two components. The real parameter  $\mu$  denotes the average mass of the mixture, and the two remaining parameters  $\epsilon > 0$  and  $\sigma \geq 0$  are dimensionless interaction lengths. Without going into detail,  $\epsilon > 0$  being small corresponds to short range repulsions between the monomers being strong, inducing a strong compulsion to separate. In contrast,  $\sigma > 0$  being large represents strong long range chain elasticity forces, which induces a strong compulsion to hold together. The diblock copolymer model (2) is an extension of the celebrated Cahn-Hilliard equation [6], which corresponds to the special case  $\sigma = 0$  and serves as a fundamental model for the phase separation phenomena spinodal decomposition [31, 32, 45, 46, 53] and nucleation [3, 4, 18].

As a physical model which is the gradient of an associated energy, the long-term dynamics of the diblock copolymer equation can be described through its global attractor. This is a compact set in phase space towards which every single solution of the evolution equation (2) converges as  $t \rightarrow \infty$ . The existence of this global attractor can be established using the techniques of [48]. Moreover, one

can show that the attractor is a finite-dimensional subset of the infinite-dimensional phase space of the equation, and that for generic parameter values of the model it contains finitely many equilibrium solutions of the diblock copolymer model, i.e., solutions of the evolution equation which do not change in time. Apart from these stationary states, the attractor consists of heteroclinic solutions which describe transitional behavior. The latter are nonconstant solutions  $u(t)$  which exist for all times  $t$ , and which converge to different equilibrium solutions as  $t \rightarrow \pm\infty$ . Based on this, the global long-term behavior of the equation can be described completely, if one has complete knowledge of the set of equilibria and the heteroclinic connections between them.

Describing the complete attractor in a mathematically rigorous manner has proven to be elusive, even for the Cahn-Hilliard special case  $\sigma = 0$ . While the equilibrium structure of the Cahn-Hilliard equation is completely known for one-dimensional base domains [21], the precise structure of heteroclinic connections is an open question and has been answered only partially [4, 22]. Even for special two-dimensional domains such as the unit square, the overall equilibrium structure of the Cahn-Hilliard equation is extremely complex, with hundreds of equilibria for moderately large  $\epsilon$ -values. Rigorous mathematical results in two dimensions therefore concentrate on specific solutions, or very specific parameter regimes, see for example [19, 30] and the references therein. In addition, computer-assisted proof techniques have been used to verify the equilibrium structure for parameter intervals on which the attractor is still small [28], and in these cases one could also partially uncover the structure of heteroclinic orbits using Conley index techniques [29]. But apart from these first results, studying the attractor structure of the Cahn-Hilliard equation on two-dimensional domains remains an open and challenging problem. In the case of the full diblock copolymer model, i.e., for  $\sigma > 0$ , even less is known. There are mathematical results on specific types of equilibrium solutions for two- and three-dimensional domains  $\Omega$ , see for example [41, 42, 43, 44] as well as the references therein. Moreover, numerical studies have been performed of the long-term behavior of solutions of (2) which originate close to the homogeneous state [8, 9].

For the purposes of the present paper, we focus exclusively on the diblock copolymer model on one-dimensional domains  $\Omega$ . At first glance, at least the structure of the equilibrium set should be within reach of a rigorous mathematical treatment, since the diblock copolymer model for small  $\sigma > 0$  is a regular perturbation of the Cahn-Hilliard model, and for the latter the equilibrium structure is described completely in [21]. Yet, the proof techniques used in that work are based on phase plane methods, and while they can be used in the Cahn-Hilliard setting, which allows for a reduction to a second-order equation, the full diblock copolymer model cannot be treated in this way.

Recent numerical studies in [24] have demonstrated that the structure of the equilibrium set is considerably richer for  $\sigma > 0$ , even for small values of the parameter. This is visualized in Figure 1, which contains equilibrium bifurcation diagrams for the parameter values  $\sigma = 0, 3, 6$ , and  $9$ , from top left to bottom right, and for total mass  $\mu = 0$  and domain  $\Omega = (0, 1)$ . Each diagram indicates the structure of the equilibrium set as a function of the new parameter  $\lambda = 1/\epsilon^2$ . As we mentioned earlier, the interesting regime is the limit  $\epsilon \rightarrow 0$ , and by switching to  $\lambda$  the diagrams become easier to visualize. In the diagrams, each colored point corresponds to at least one stationary solution of the diblock copolymer model, and the color indicates the Morse index of the equilibrium in the evolution equation (2), as described in the figure caption. The horizontal straight lines in all images represent the constant function  $u \equiv \mu = 0$ , which is clearly an equilibrium, and which we call the *trivial solution*. As  $\lambda$  increases, nontrivial solutions bifurcate from the trivial branch in pairs, even though we only plot one of these branches. This is due to the fact that the vertical axes of the bifurcation diagrams show the  $L^2(\Omega)$ -norm of the stationary state, and the bifurcation pairs are related by a norm-preserving symmetry.

For the Cahn-Hilliard case  $\sigma = 0$ , i.e., in the top left bifurcation diagram, pairs of solutions are created at the bifurcation points  $\lambda = k^2\pi^2$  for  $k \in \mathbb{N}$ , and the solutions on the  $k$ -th branch look qualitatively similar to the function  $\cos(k\pi x)$ . In this case, each nontrivial solution branch corresponds

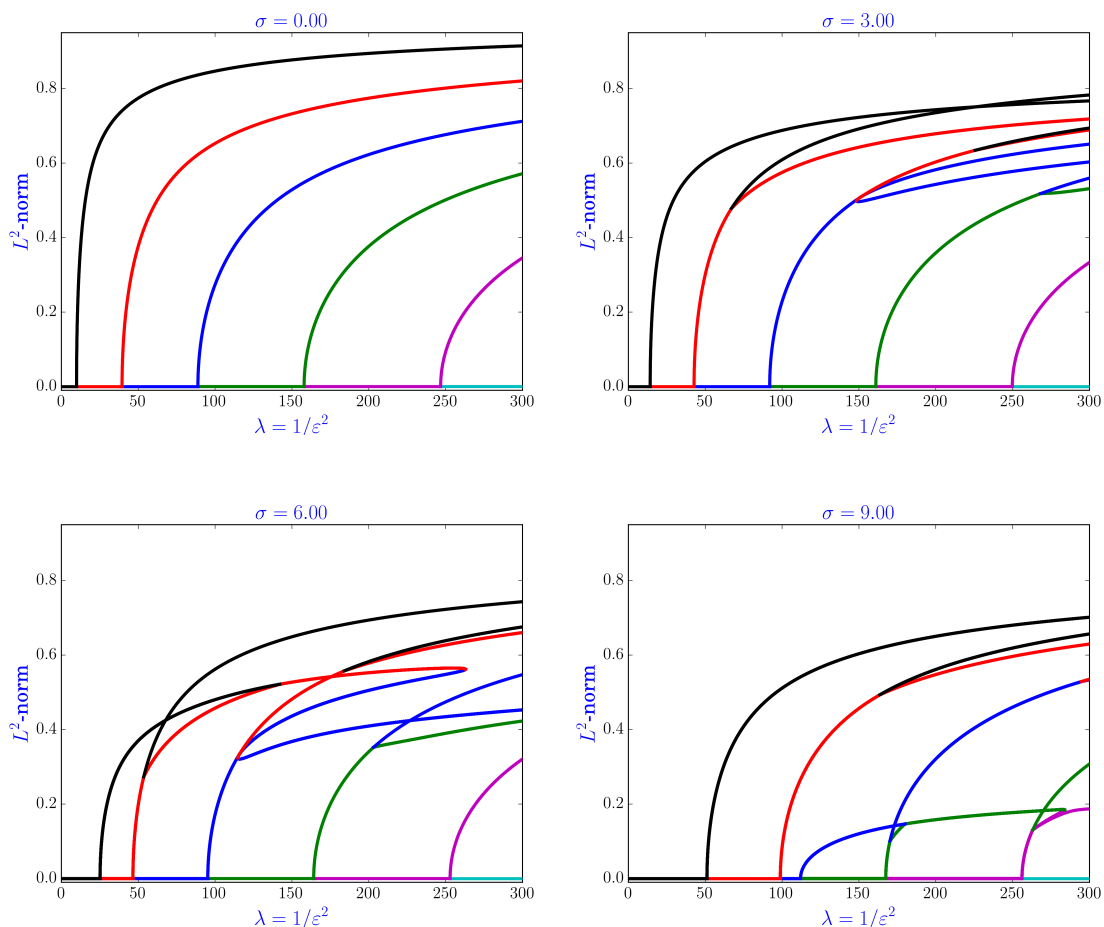


Figure 1: Bifurcation diagrams for the diblock copolymer model (2) on the domain  $\Omega = (0, 1)$  and for total mass  $\mu = 0$ . From top left to bottom right the bifurcation diagrams are for  $\sigma = 0, 3, 6,$  and  $9$ , respectively. In each diagram, the vertical axis measures the  $L^2(0, 1)$ -norm of the solutions, and the horizontal axis uses the parameter  $\lambda = 1/\epsilon^2$ . The solution branches are color-coded by the Morse index of the solutions, and black, red, blue, green, magenta, and cyan correspond to indices 0, 1, 2, 3, 4, and 5, respectively.

to exactly two nontrivial solutions. It was shown in [21] that there are no other equilibrium solutions for the equation, i.e., none of the bifurcation branches exhibit secondary bifurcations. Moreover, only the solutions on the first branch are stable equilibria, and they correspond to solutions with one transition layer. The situation changes dramatically for  $\sigma > 0$ . In the diblock copolymer case, all branches which are created at the trivial solution exhibit secondary bifurcations. Even more importantly, these secondary bifurcations can lead to the creation of multiple stable equilibrium solutions. While as of yet there are no classical mathematical proofs for these statements, computer-assisted proof methods were developed in [56], which allow for the validation of these equilibrium branches. See also the work in [47, 54]. Some first results for two-dimensional domains can be found in the recent paper [52].

But how does this multistability manifest itself in the evolution equation (2)? Based on the underlying physical situation, one is usually interested in studying the long-term behavior of solutions of the diblock copolymer model which originate close to the (unstable) homogeneous equilibrium state  $u \equiv \mu$ . These long-term limits are usually periodic with a specific period which depends on the precise parameter combinations. Since the system exhibits multiple stable states which all are at least local minimizers of the energy, it is natural to wonder whether typical solutions converge to the global

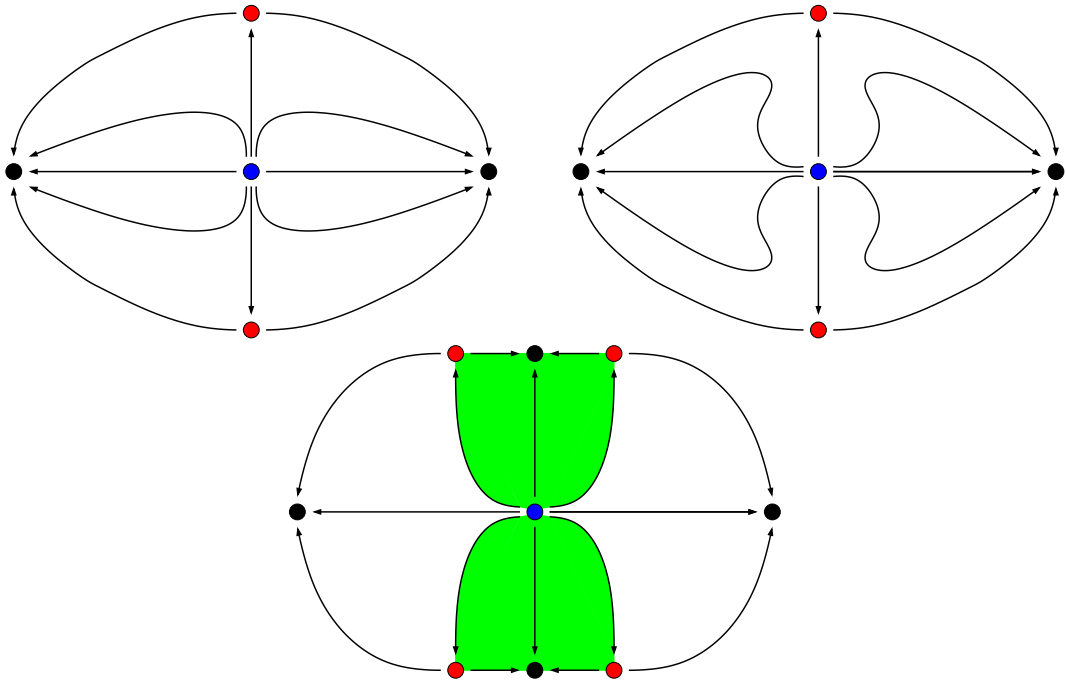


Figure 2: Heuristic explanation for the numerical observation that most solutions of the diblock copolymer model which start close to the homogeneous state will converge to the local energy minimizer, rather than the global energy minimum. From top left to bottom the images provide simplified schematics for part of the attractor, for increasing values of the bifurcation parameter  $\lambda = 1/\epsilon^2$ . While in the top left image only the global minimizers exist (black dots), one first encounters a tangency change of solutions close to the homogeneous state (blue dot), before at last the new stable equilibria bifurcate.

energy minimizers or are trapped earlier. A systematic numerical study of this long-term behavior was performed in [24]. In this paper, a large number of Monte-Carlo type simulations were used to create a subdivision of the positive  $\lambda$ - $\sigma$ -quadrant in terms of the periodicity of the observed long-term limit of most solutions starting near the homogeneous state. These simulations led to two significant observations:

- First of all, the periodicity of the long-term limit, i.e., of the trapping local energy minimizer, changes abruptly across well-delineated curves in the positive  $\lambda$ - $\sigma$ -quadrant. Furthermore, the observed periodicity of this limit is considerably higher than the actual periodicity of the global energy minimizers. An asymptotic formula for the latter period had been derived in [40].
- In addition, the delineating curves at which the observed periodicity of the long-term limit changes can be related to the location curves of particular secondary bifurcations from a nontrivial solution branch in the equilibrium diagram. These secondary bifurcation points are pitchfork bifurcations which create new stable equilibria. In the upper right and lower left diagrams of Figure 1 these bifurcation points can be found on the red branch which originates at the trivial solution. For  $\sigma = 3$  this occurs at  $\lambda \approx 67.1$ , and for  $\sigma = 6$  we have  $\lambda \approx 53.6$ . In other words, the two points  $(\lambda, \sigma) = (67.1, 3)$  and  $(\lambda, \sigma) = (53.6, 6)$  lie on one of these sharp delineating curves in the positive  $\lambda$ - $\sigma$ -quadrant.

But why would a local pitchfork bifurcation which happens far away from the trivial solution have an immediate effect on the long-term limits of solutions of (2) starting close to this homogeneous

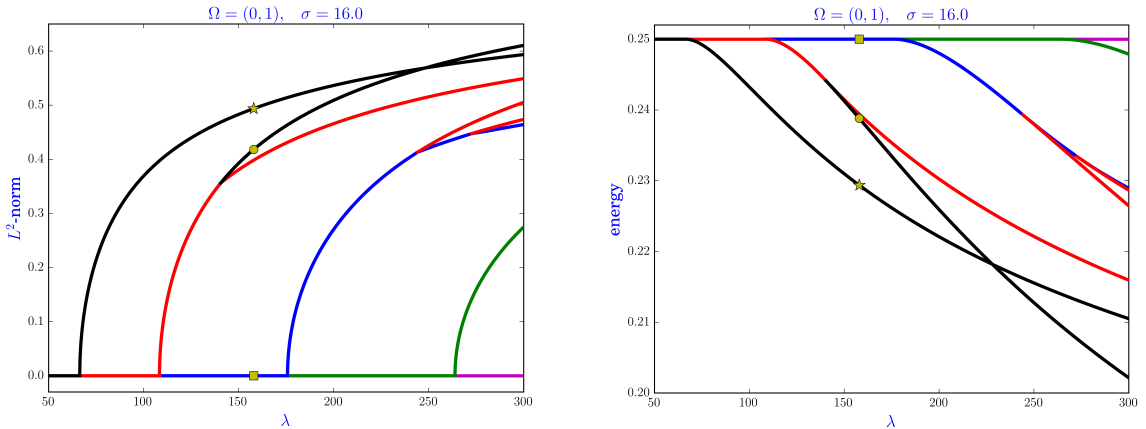


Figure 3: Bifurcation diagrams for the diblock copolymer model (2) on the domain  $\Omega = (0, 1)$ , for total mass  $\mu = 0$ , and for nonlocal interaction parameter  $\sigma = 16$ . In the left diagram, the vertical axis measures the  $L^2(0, 1)$ -norm of the solutions, while the right diagram shows the total energy (1). In both diagrams, the horizontal axis uses the parameter  $\lambda = 1/\epsilon^2$ . As in Figure 1, the solution branches are color-coded by the Morse index of the solutions, and black, red, blue, green, and magenta correspond to indices 0, 1, 2, 3, and 4, respectively.

state? From a purely intuitive perspective, it is not very difficult to imagine why certain local energy minimizers could in fact be the long-term limit of many solutions originating close to the homogeneous state, and a heuristic explanation for this trapping of most solutions was proposed in [55]. To explain this in more detail, we refer the reader to the panels of Figure 2. In these images, the blue dot indicates the homogeneous equilibrium, red dots are index one stationary states, and black dots correspond to stable states. From top left to lower middle, the images are for increasing values of  $\lambda$ . While initially most solutions starting near the center are directed towards the black stable equilibria (top left image), the local instabilities change in order to direct most solutions to the unstable red ones (top right image). Once the latter equilibria undergo a secondary bifurcation, most solutions originating near the center are trapped by the newly formed stable states (lower image).

While the heuristics given in [55] seems plausible, there has been no mathematical result which shows that large numbers of solutions of the diblock copolymer model which start near the trivial equilibrium solution are in fact trapped by a local energy minimizer, and that at the same time the global energy minimizers can be reached from the homogeneous state as well. It is the goal of the present paper to close this gap for the bifurcation diagram shown in Figure 3. This will be accomplished using a computer-assisted proof technique, and it will establish the existence of heteroclinic solutions between the homogeneous state and the local minimizers, as well as between the homogeneous state and the global minimizers. More precisely, we verify heteroclinic connections between the state indicated by a yellow square, to both the equilibria indicated by yellow circles and the equilibria indicated by a yellow star.

In recent years, computer-assisted proof techniques have been used extensively in the context of nonlinear partial differential equations, and they are based on a number of different approaches. Our results in the present paper are based on the concept of *self-consistent bounds*, see for example [2, 14, 15, 60, 61, 62, 64]. Thus, our approach differs in spirit from techniques based on Newton-Kantorovich type arguments in a functional analytic setting, which were used for example in [7, 20, 50]. To perform the necessary rigorous time integration, we make use of the fast algorithm proposed in [11]. We would like to mention that establishing the existence of connecting orbits in finite-dimensional continuous and discrete dynamical systems has been the subject of a number of studies, see for example [23, 50, 57, 58, 59]. In addition, the global dynamics of the Swift-Hohenberg model has been

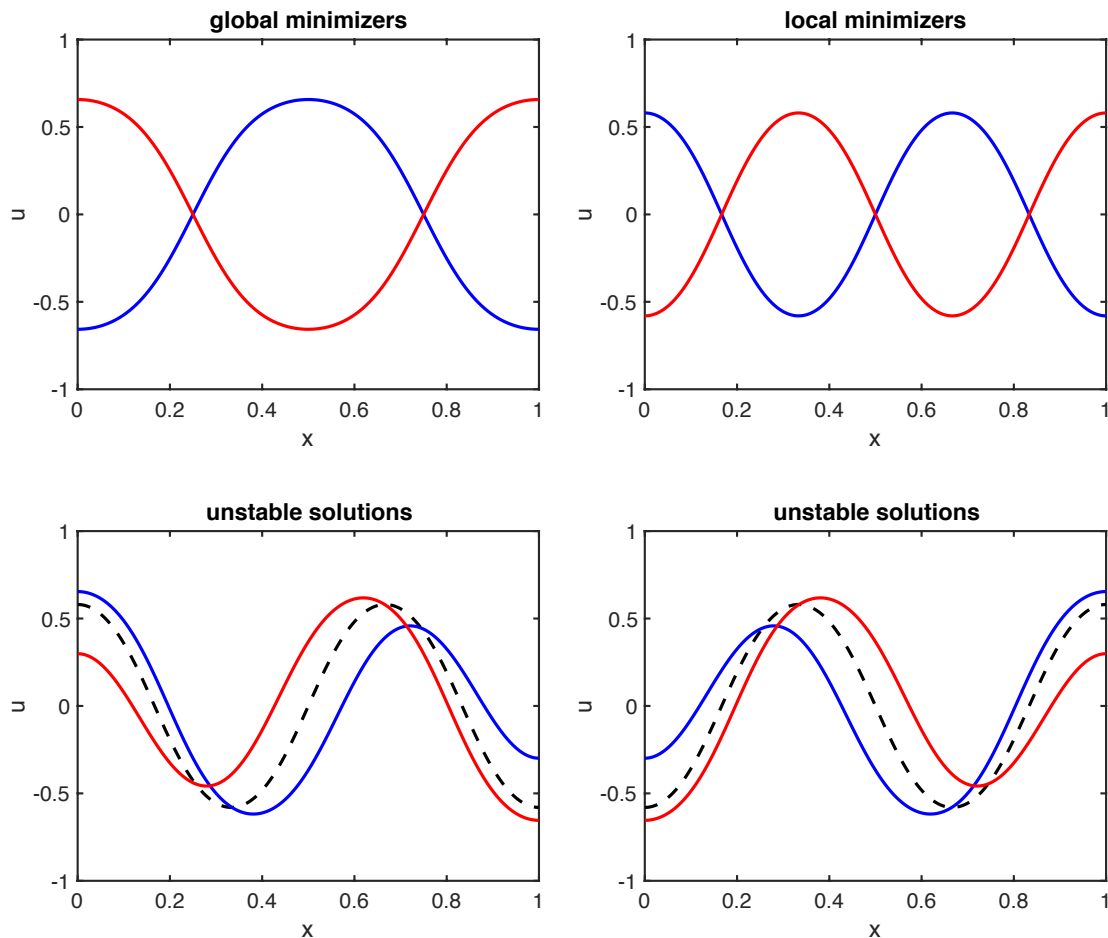


Figure 4: Stationary solutions of the diblock copolymer model (2) on the domain  $\Omega = (0, 1)$ , for total mass  $\mu = 0$ , and for interaction length parameters  $\lambda = 16\pi^2 \approx 157.91$  and  $\sigma = 16$ . The top left image contains the two global energy minimizers, which are indicated by a star in the bifurcation diagrams of Figure 3. The image in the top right shows the local energy minimizers, which are marked by circles in Figure 3. The two bottom panels show the index one solutions which are created through a stabilizing pitchfork bifurcation. In each figure, the local minimizer from the respective primary bifurcation branch is shown as a dashed black curve.

uncovered using a Morse decomposition based approach in [17], and the existence of periodic orbits for the ill-posed Boussinesq equation was established in [7, 15]. Finally, the existence of a heteroclinic orbit between the trivial and a nontrivial stationary state has been established for the one-dimensional  $p$ -Laplace equation in [67]. To achieve this result, the authors use purely analytical techniques which are based on the Conley index, and which cannot be easily applied in the situation of the present paper. Also, Zgliczyński could verify the existence of a heteroclinic connection in the Kuramoto-Sivashinsky equation using similar techniques in the recent preprint [65].

The results of this paper are formulated for a specific situation, which is motivated by the numerical results of [24]. It was shown in this work that on the one-dimensional domain  $\Omega = (0, 1)$  and for parameters  $\mu = 0$ ,  $\sigma = 16$  and  $\lambda = 1/\epsilon^2 \approx 140$ , the diblock copolymer model (2) exhibits multistability which can be observed in practice. More precisely, if one randomly chooses initial conditions near the homogeneous state  $u \equiv \mu = 0$ , then some of the resulting solutions converge to the global energy minimizer, while some are trapped in a local energy minimum. Thus, the basis of the present paper is the bifurcation diagram shown in the left panel of Figure 3, which is for the interaction length  $\sigma = 16$ .

The right panel in the figure depicts the same bifurcation diagram, but this time the vertical axis is given by the energy (1) of the equilibrium solutions. For our proof, we consider the specific parameter value  $\lambda = 16\pi^2 \approx 157.91$ , which falls further into the regime discussed in [24]. At this value, the diblock copolymer model has eight nontrivial equilibrium solutions, which are shown in Figure 4. The top left image shows the two global energy minimizers, which are marked by a star in Figure 3, while the two local minimizers are indicated by a yellow circle, and are shown in the top right panel of Figure 4. Finally, the four colored solutions in the two lower panels of Figure 4 are of index one, and they all lie on the red secondary bifurcation branch in Figure 3. We would like to point out that the equilibrium solutions on the first and second branch bifurcating from the horizontal trivial solution line have two and three transition layers, respectively. While the reason for this is described in more detail in [24], it is due to the fact that as  $\sigma$  increases from zero, the left-most branch shown in the top left bifurcation diagram of Figure 1 starts moving to the right, interacts with all subsequent branches, and then disappears at  $\lambda = \infty$  for  $\sigma = \pi^2$ . Thus, for  $\sigma = 16 > \pi^2$ , we obtain the above-mentioned periodicities of the stationary states. Our main result can then be stated as follows.

**Theorem 1.1** (Existence of heteroclinic connections). *Consider the diblock copolymer equation (2) on the one-dimensional domain  $\Omega = (0, 1)$ , for interaction lengths  $\lambda = 1/\epsilon^2 = 16\pi^2$  and  $\sigma = 16$ , and for total mass  $\mu = 0$ . Then there exist heteroclinic connections between the unstable homogeneous stationary state  $u \equiv \mu$  and each of the two local energy minimizers which are indicated by yellow circles in Figure 3, and shown in the top right panel of Figure 4. In addition, there exist heteroclinic connections between the unstable homogeneous stationary state and each of the two global energy minimizers which are indicated by yellow stars in Figure 3, and which are shown in the top left panel of Figure 4. In other words, for the above parameter values the diblock copolymer equation (2) exhibits multistability in the sense that all local or global energy minimizers can be reached from the homogeneous state.*

The above theorem will be established as Theorem 4.1, which for computational reasons considers a rescaled version of the diblock copolymer model. To the best of our knowledge, this is the first result which rigorously establishes that not all solutions of (2) which originate close to the homogeneous state converge to the global energy minimizer. In fact, the proof of our result below shows that there are infinitely many orbits which are trapped by each of the two local and of the two global energy minimizers. Notice that this result cannot easily be obtained by methods based on Conley’s connection matrix. As the latter is a degree minus one map, it can only be used to verify isolated heteroclinics between equilibrium solutions whose index differs by one. In our situation, we establish heteroclinic solutions between an index two equilibrium and stable stationary states.

The remainder of the paper is organized as follows. In Section 2 we describe the general setting for our approach, while Section 3 is devoted to its theoretical foundations. We recall basic definitions and results for isolating blocks, self-consistent bounds, as well as the cone condition. Based on this, Section 4 contains the proof of our main theorem. The next three sections are concerned with the computational aspects of our work. While the rigorous integration algorithm is described in Section 5, the following Section 6 shows how the cone condition can be verified in infinite dimensions. General remarks about the software can be found in Section 7. Section 8 contains conclusions and future plans. Finally, Appendix A.1 contains some numerical data from the computer assisted part of the proof.

## 2 Problem formulation and basic setting

We begin by presenting the basic setup for our computer-assisted proof. As was mentioned in the introduction, our goal is to consider the diblock copolymer model (2) on the domain  $\Omega = (0, 1)$ . Unfortunately, for the parameter range of interest this choice of domain leads to extreme stiffness in the discretized equations. We will address this issue through rescaling techniques, and as a consequence

our basic setup will be for a general one-dimensional domain of the form  $\Omega = (0, L)$ . The length  $L$  will be chosen later in such a way to reduce the stiffness of the problem. Thus, we study problem (2) in one dimension in the form

$$u_t = - (u_{xx} + \lambda f(u))_{xx} - \lambda \sigma(u - \mu), \quad (3)$$

which is equivalent to (2) up to a rescaling of time. In this formulation, we use the parameter  $\lambda = 1/\epsilon^2$ , and consider the partial differential equation subject to the mass and boundary constraints given by

$$\mu = \frac{1}{L} \int_0^L u(t, x) dx \quad \text{and} \quad u_x(t, x) = u_{xxx}(t, x) = 0 \quad \text{for} \quad t > 0, \quad x \in \{0, L\}.$$

As before, the nonlinearity is given by  $f(u) = u - u^3$ , and we consider the case  $\mu = 0$  of zero total mass, which means that we have equal amounts of the two polymers A and B.

Our basic discretization of this infinite-dimensional problem is based on the Fourier series expansion. More precisely, due to the imposed homogeneous Neumann boundary conditions we consider the expansion

$$u(t, x) = a_0(t) + 2 \sum_{k=1}^{\infty} a_k(t) \cos \frac{\pi k x}{L}, \quad (4)$$

which is based on the *cosine Fourier basis*. We would like to point out that due to our choice  $\mu = 0$  for the total mass we automatically have

$$a_0(t) = 0 \quad \text{for all} \quad t \geq 0.$$

Notice also that the domain length  $L$  enters the expansion. We will see later that by choosing  $L$  large enough the stiffness of the problem (3) can be reduced, since the eigenvalues of the linear part of a suitable finite-dimensional approximation are more averaged. To simplify notation, we will use the abbreviation

$$e_k(x) := \cos \frac{\pi k x}{L}, \quad \text{where} \quad k \geq 0,$$

for the basis functions in the above expansion. By default we assume that the coefficients  $a_k$  are dependent on time  $t$ , and we therefore frequently drop the explicit mentioning of the temporal argument. Upon substituting the series representation of  $u$  into the cubic part of the nonlinearity  $f$  one obtains

$$\begin{aligned} u^3 &= \left( 2 \sum_{k \geq 1} a_k e_k(x) \right)^3 = 8 \sum_{j_1 \geq 1} \sum_{j_2 \geq 1} \sum_{j_3 \geq 1} a_{j_1} a_{j_2} a_{j_3} \cdot \cos \frac{\pi j_1 x}{L} \cdot \cos \frac{\pi j_2 x}{L} \cdot \cos \frac{\pi j_3 x}{L} \\ &= 2 \sum_{j_1, j_2, j_3 \geq 1} a_{j_1} a_{j_2} a_{j_3} \left( \cos \frac{\pi}{L} (j_1 - j_2 - j_3)x + \cos \frac{\pi}{L} (j_1 + j_2 - j_3)x \right. \\ &\quad \left. + \cos \frac{\pi}{L} (j_1 - j_2 + j_3)x + \cos \frac{\pi}{L} (j_1 + j_2 + j_3)x \right). \end{aligned}$$

The last expression can be further simplified using the fact that

$$\cos \frac{\pi k x}{L} = \frac{1}{2} \left( \exp \frac{i \pi k x}{L} + \exp \frac{-i \pi k x}{L} \right),$$

which implies that

$$\begin{aligned}
u^3 &= \sum_{j_1, j_2, j_3 \geq 1} a_{j_1} a_{j_2} a_{j_3} \left( \exp \frac{i\pi(j_1 - j_2 - j_3)x}{L} + \exp \frac{i\pi(-j_1 + j_2 + j_3)x}{L} + \right. \\
&\quad \exp \frac{i\pi(j_1 + j_2 - j_3)x}{L} + \exp \frac{i\pi(-j_1 - j_2 + j_3)x}{L} + \\
&\quad \exp \frac{i\pi(j_1 - j_2 + j_3)x}{L} + \exp \frac{i\pi(-j_1 + j_2 - j_3)x}{L} + \\
&\quad \left. \exp \frac{i\pi(j_1 + j_2 + j_3)x}{L} + \exp \frac{i\pi(-j_1 - j_2 - j_3)x}{L} \right) \\
&= \sum_{j_1, j_2, j_3 \in \mathbb{Z}} a_{j_1} a_{j_2} a_{j_3} \cdot \exp \frac{i\pi(j_1 + j_2 + j_3)x}{L} = \sum_{k \in \mathbb{Z}} \sum_{\substack{j_1, j_2, j_3 \in \mathbb{Z} \\ j_1 + j_2 + j_3 = k}} a_{j_1} a_{j_2} a_{j_3} \cdot \exp \frac{i\pi kx}{L},
\end{aligned}$$

as long as we recall  $a_0 = 0$  and define  $a_{-k} = a_k$  for  $k \in \mathbb{N}$ . By reordering the outer sum, one further obtains

$$\begin{aligned}
u^3 &= \sum_{\substack{j_1, j_2, j_3 \in \mathbb{Z} \\ j_1 + j_2 + j_3 = 0}} a_{j_1} a_{j_2} a_{j_3} + \sum_{k \in \mathbb{N}} \sum_{\substack{j_1, j_2, j_3 \in \mathbb{Z} \\ j_1 + j_2 + j_3 = k}} a_{j_1} a_{j_2} a_{j_3} \cdot \left( \exp \frac{i\pi kx}{L} + \exp \frac{-i\pi kx}{L} \right) \\
&= \sum_{\substack{j_1, j_2, j_3 \in \mathbb{Z} \\ j_1 + j_2 + j_3 = 0}} a_{j_1} a_{j_2} a_{j_3} + 2 \sum_{k \in \mathbb{N}} \left( \sum_{\substack{j_1, j_2, j_3 \in \mathbb{Z} \\ j_1 + j_2 + j_3 = k}} a_{j_1} a_{j_2} a_{j_3} \right) \cos \frac{\pi kx}{L}
\end{aligned}$$

If we finally substitute this expression for  $u^3$ , together with the original series expansion for  $u$ , into the differential equation (3), then one obtains after division by 2 and extraction of the coefficients of the basis functions  $e_k(x)$  the identities

$$\frac{da_k}{dt} = \left( -\frac{k^4 \pi^4}{L^4} + \frac{\lambda k^2 \pi^2}{L^2} - \lambda \sigma \right) a_k - \frac{\lambda k^2 \pi^2}{L^2} \sum_{\substack{j_1, j_2, j_3 \in \mathbb{Z} \\ j_1 + j_2 + j_3 = k}} a_{j_1} a_{j_2} a_{j_3} \quad \text{for all } k \geq 0. \quad (5)$$

In this way, we have reformulated the original parabolic partial differential equation as an infinite system of ordinary differential equations. This system will be used throughout the remainder of the paper. Recall one more time that the coefficient sequence  $a_k$  satisfies

$$a_0 = 0, \quad \text{as well as } a_k = a_{-k} \in \mathbb{R} \quad \text{for all } k \in \mathbb{Z}.$$

To close this section, we present two central definitions. The first one is concerned with the function space which forms the basis of our computer-assisted proof.

**Definition 2.1** (Sequence space with algebraic coefficient decay). *Let  $H$  denote the space  $\ell^2(\mathbb{Z}, \mathbb{R})$ , i.e., elements  $a \in H$  are sequences  $a: \mathbb{Z} \rightarrow \mathbb{R}$  such that  $\sum_{k \in \mathbb{Z}} |a_k|^2 \leq \infty$ . In addition, let  $\tilde{H} \subset H$  denote the subspace of  $H$  which is defined by*

$$\tilde{H} := \left\{ \{a_k\}_{k \in \mathbb{Z}} \in H : \text{there exists a constant } C \geq 0 \text{ such that } |a_k| \leq \frac{C}{\dagger k \dagger^6} \text{ for } k \in \mathbb{Z} \right\},$$

where  $\dagger x \dagger = |x|$  for  $x \neq 0$  and  $\dagger 0 \dagger = 1$ . Finally, let the space  $H'$  be given by

$$H' := \tilde{H} \cap \{ \{a_k\}_{k \in \mathbb{Z}} : a_0 = 0 \text{ and } a_k = a_{-k} \text{ for all } k \in \mathbb{Z} \}.$$

Notice that all three spaces are Hilbert spaces.

From now on, all computations we perform in infinite dimensions will be constrained to the space  $H'$ . Needless to say, any actual numerical computations performed on a computer have to take place in finite dimensions, and for this we make use of *Galerkin approximations* of (5), which are the subject of the following final definition of this section.

**Definition 2.2** (Galerkin approximation). *Consider the infinite system of ordinary differential equations given in (5), and let  $n \in \mathbb{N}$  be arbitrary. Then the  $n$ -th Galerkin approximation of (5) is defined as*

$$\frac{da_k}{dt} = \left( -k^2 \left( \frac{\pi}{L} \right)^2 \left( k^2 \left( \frac{\pi}{L} \right)^2 - \lambda \right) - \lambda \sigma \right) a_k - \lambda k^2 \left( \frac{\pi}{L} \right)^2 \sum_{\substack{|j_1|, |j_2|, |j_3| \leq n \\ j_1 + j_2 + j_3 = k}} a_{j_1} a_{j_2} a_{j_3}, \quad (6)$$

for any coefficient index  $k = 1, \dots, n$ . In other words, the  $n$ -th Galerkin approximation is an  $n$ -dimensional system of ordinary differential equations, which depends only on the coefficients  $a_1, \dots, a_n$ .

### 3 Isolating blocks, self-consistent bounds, and the cone condition

In this section we briefly recall the theoretical framework that is used to establish the main result of this paper. More precisely, we review the concepts of *cone conditions* and *self-consistent bounds* as introduced by Zgliczyński. In Section 3.1, we present a finite-dimensional version of *h-sets*, *isolating blocks*, and *cone conditions*. This is followed in Section 3.2 by a discussion of *self-consistent bounds*, which allows one to extend the notion of *h-sets*, *isolating blocks*, and *cone conditions* to the Hilbert space setting. Finally, in Section 3.3 we present the concept of infinite-dimensional cone conditions, i.e. we show how to verify cone conditions on infinite-dimensional self-consistent bounds. Since the results presented in this section are known, our presentation will be short, albeit as self-contained as possible. For more detailed discussions of *h-sets*, *isolating blocks*, and *cone conditions* we refer the reader to [59, 63, 66], and references therein.

The concepts introduced in the present section will be used in two different ways in the proof of our main theorem, which is the subject of the next Section 4. On the one hand, we use the fact that the construction of an *unstable* infinite-dimensional isolating block which satisfies a cone condition provides us with explicit bounds for the unstable manifold of the unstable steady state contained in the block. On the other hand, the construction of a *stable* infinite-dimensional isolating block which satisfies a cone condition guarantees the local uniqueness of the stable stationary solution contained in the block, as well as explicit bounds for the size of its basin of attraction.

#### 3.1 Isolating blocks and cone conditions in finite dimensions

We begin by reviewing the concepts of isolating blocks and cone conditions in a finite-dimensional setting. For this, let  $n \in \mathbb{N}$  be arbitrary. Then for any vector  $z \in \mathbb{R}^n$  we let  $\|z\|$  denote a norm on  $\mathbb{R}^n$ , which does not have to be the standard Euclidean norm. The basic types of sets necessary for our discussion are interval sets. For this, consider real numbers  $x_k^\pm$  for  $k = 1, \dots, n$ . Then we define the *interval set*  $[x]$  by

$$[x] = \prod_{k=1}^n [x_k^-, x_k^+] \subset \mathbb{R}^n, \quad \text{as long as} \quad x_k^- \leq x_k^+ \quad \text{for} \quad k = 1, \dots, n.$$

For any point  $x_0 \in \mathbb{R}^n$  and arbitrary  $r > 0$ , we let  $B_n(x_0, r) = \{z \in \mathbb{R}^n \mid \|z - x_0\| < r\}$  denote the open ball of radius  $r$  centered at  $x_0$ , and we use the abbreviation  $B_n = B_n(0, 1)$  for the unit ball centered at the origin. For a linear map  $A: \mathbb{R}^n \rightarrow \mathbb{R}^n$ , we let  $Sp(A)$  denote the spectrum of  $A$ . When considering product spaces such as  $\mathbb{R}^u \times \mathbb{R}^s$ , we write elements  $z \in \mathbb{R}^u \times \mathbb{R}^s$  in the form  $z = (x, y)$ , where  $x \in \mathbb{R}^u$  and  $y \in \mathbb{R}^s$  denote the first and second component vectors of  $z$ , respectively. Moreover,

if  $f: \mathbb{R}^n \rightarrow \mathbb{R}^n$  denotes a continuously differentiable function, and if  $Z \subset \mathbb{R}^n$  is a compact set, then we define

$$[df(Z)] = \left\{ M = (M_{ij})_{i,j=1}^n \in \mathbb{R}^{n \times n} \mid M_{ij} \in \left[ \inf_{z \in Z} \frac{\partial f_i}{\partial x_j}(z), \sup_{z \in Z} \frac{\partial f_i}{\partial x_j}(z) \right] \right\} .$$

Consider now an ordinary differential equation of the form

$$z' = f(z), \quad z \in \mathbb{R}^n, \quad f \in C^2(\mathbb{R}^n, \mathbb{R}^n). \quad (7)$$

Then we denote by  $\varphi(t, z_0)$  the solution of (7) which satisfies the initial condition  $z(0) = z_0$ . Notice that since we assume the twice continuous differentiability of  $f$ , the solution of this initial value problem is in fact uniquely determined.

After these preparations, we now turn our attention to the concept of  $h$ -sets. Informally speaking, an  $h$ -set is a subset of Euclidean space, which becomes a cube after a suitable choice of coordinate system. In addition, the letter  $h$  alludes to the fact that this choice of coordinate system will lead to a phase portrait for the underlying ordinary differential equation which exhibits typical hyperbolic-like form. The concept of  $h$ -sets originated in the work on covering relations for multi-dimensional dynamical systems, see [66]. From the perspective of our specific application, the considered  $h$ -sets have a trivial structure in the sense that the cube is always expressed with respect to canonical coordinates. Consequently, also the cone conditions which will be introduced below are expressed in the canonical coordinate system. More precisely, in our application to the unstable homogeneous state, two of the dimensions will be distinguished as unstable, while the homeomorphism  $c_N$  appearing in the following definition of an  $h$ -set is just a scaling. Despite this fact, we now recall the appropriate definitions in their original form.

**Definition 3.1** ( *$h$ -set [66, Definition 1]*). *An  $h$ -set is a quadruple of the form  $(N, u(N), s(N), c_N)$  which satisfies the following three conditions:*

- *The set  $N$  is a compact subset of  $\mathbb{R}^n$ ,*
- *the natural numbers  $u(N), s(N) \in \mathbb{N}_0$  satisfy the identity  $u(N) + s(N) = n$ , and*
- *the mapping  $c_N: \mathbb{R}^n \rightarrow \mathbb{R}^n$ , where we write  $\mathbb{R}^n = \mathbb{R}^{u(N)} \times \mathbb{R}^{s(N)}$ , is a homeomorphism which satisfies*

$$c_N(N) = \overline{B_{u(N)}} \times \overline{B_{s(N)}} .$$

*In the following, we will slightly abuse notation and refer to an  $h$ -set as just  $N$ , rather than always listing the full quadruple. In addition, with each  $h$ -set we associate the sets*

$$\begin{aligned} N_c^- &:= \partial B_{u(N)} \times \overline{B_{s(N)}}, & N_c^+ &:= \overline{B_{u(N)}} \times \partial B_{s(N)}, & N_c &:= \overline{B_{u(N)}} \times \overline{B_{s(N)}}, \\ N^- &:= c_N^{-1}(N_c^-), & N^+ &:= c_N^{-1}(N_c^+), \end{aligned}$$

*and we define  $\dim(N) := n$ .*

The above definition shows that an  $h$ -set  $N$  is the product of two closed unit balls in some appropriate coordinate system. The two integers  $u(N)$  and  $s(N)$  are called the *nominally unstable* and *nominally stable dimensions*, respectively. The subscript  $c$  refers to the new coordinates given by the homeomorphism  $c_N$ . Note that if we have  $u(N) = 0$ , then one immediately obtains  $N^- = \emptyset$ , and the identity  $s(N) = 0$  implies  $N^+ = \emptyset$ . The next definition introduces the concept of a horizontal disk.

**Definition 3.2** (Horizontal disk [59, Definition 10]). *Let  $N$  denote an arbitrary  $h$ -set. In addition, consider a continuous mapping  $b: \overline{B_{u(N)}} \rightarrow N$ , and define  $b_c = c_N \circ b$ . Then we say that  $b$  is a horizontal disk in  $N$ , if there exists a homotopy  $h: [0, 1] \times \overline{B_{u(N)}} \rightarrow N_c$  such that*

$$\begin{aligned} h(0, x) &= b_c(x) & \text{for all } x &\in \overline{B_{u(N)}}, \\ h(1, x) &= (x, 0) & \text{for all } x &\in \overline{B_{u(N)}}, \\ h(t, x) &= N_c^- & \text{for all } t &\in [0, 1] \text{ and } x \in \partial B_{u(N)}. \end{aligned}$$

In order to handle the hyperbolic structure of  $h$ -sets, we use the notion of *cones*, which are defined through a quadratic form defined on the  $h$ -set in the following way.

**Definition 3.3** ( $h$ -set with cones [66, Definition 8]). *Let  $N \subset \mathbb{R}^n$  denote an arbitrary  $h$ -set, and consider the associated splitting  $\mathbb{R}^n = \mathbb{R}^{u(N)} \times \mathbb{R}^{s(N)}$ . Furthermore, let  $Q: \mathbb{R}^{u(N)} \times \mathbb{R}^{s(N)} \rightarrow \mathbb{R}$  be a quadratic form which is given as the difference*

$$Q(x, y) = \alpha(x) - \beta(y), \quad \text{for arbitrary } (x, y) \in \mathbb{R}^{u(N)} \times \mathbb{R}^{s(N)},$$

where  $\alpha: \mathbb{R}^{u(N)} \rightarrow \mathbb{R}$  and  $\beta: \mathbb{R}^{s(N)} \rightarrow \mathbb{R}$  are positive definite quadratic forms. Then the pair  $(N, Q)$  is called an  $h$ -set with cones.

**Definition 3.4** (Cone condition [66, Definition 10]). *Consider an  $h$ -set with cones given by  $(N, Q)$ , as introduced in the previous definition. In addition, let  $b: \overline{B_{u(N)}} \rightarrow N$  denote a horizontal disk as in Definition 3.2. Then we say that  $b$  satisfies the cone condition (with respect to  $Q$ ), if and only if for arbitrary points  $x, y \in \overline{B_{u(N)}}$  we have*

$$Q(b_c(x) - b_c(y)) > 0 \quad \text{as long as } x \neq y.$$

Recall that we have  $b_c = c_N \circ b$ .

The remaining definitions of this section are concerned with standard dynamical systems notions. We begin by recalling the concept of *isolating block* from *Conley index* theory [34].

**Definition 3.5** (Isolating block). *Let  $N$  denote an arbitrary  $h$ -set. We say that  $N$  is an isolating block for the vector field  $f: \mathbb{R}^n \rightarrow \mathbb{R}^n$ , if and only if  $c_N$  is a diffeomorphism, if the sets  $N^+$  and  $N^-$  are local sections for  $f$ , i.e., the vector field  $f$  is transversal to  $N^\pm$ , and if the following two conditions are satisfied:*

- For all points  $x \in N^-$  there exists a constant  $\delta > 0$  such that  $\varphi(t, x) \notin N$  for all  $t \in (0, \delta]$ .
- For all points  $x \in N^+$  there exists a constant  $\delta > 0$  such that  $\varphi(t, x) \notin N$  for all  $t \in [-\delta, 0)$ .

In other words, the closed set  $N^-$  consists of all exit points for the flow associated with (7), and the closed set  $N^+$  is the set of entry points.

**Lemma 3.6** (Graph representation [63, Lemma 5]). *Let  $(N, Q)$  denote an arbitrary  $h$ -set with cones, and let  $b: \overline{B_{u(N)}} \rightarrow N$  be a horizontal disk which satisfies the cone condition as in Definition 3.4. Then there exists a Lipschitz continuous function  $y: \overline{B_{u(N)}} \rightarrow \overline{B_{s(N)}}$  such that  $b_c(x) = (x, y(x))$ .*

**Definition 3.7** (Hyperbolic fixed point). *Let  $z_0 \in \mathbb{R}^n$  and consider again the ordinary differential equation (7). Then  $z_0$  is called a hyperbolic fixed point for (7) if  $f(z_0) = 0$  and if  $\text{Re}\lambda \neq 0$  for all eigenvalues  $\lambda \in \text{Sp}(df(z_0))$ , where  $df(z_0)$  is the Jacobian matrix of the vector field  $f$  at the point  $z_0$ , and  $\text{Re}\lambda$  denotes the real part of the eigenvalue  $\lambda$ .*

Now consider a hyperbolic fixed point  $z_0$  which is contained in a given set  $Z \subset \mathbb{R}^n$ . Then we define the stable and unstable manifolds of  $z_0$  as

$$W_Z^s(z_0, \varphi) = \left\{ z \in Z \mid \varphi(t, z) \in Z \text{ for all } t \geq 0 \text{ and } \lim_{t \rightarrow +\infty} \varphi(t, z) = z_0 \right\} \text{ and}$$

$$W_Z^u(z_0, \varphi) = \left\{ z \in Z \mid \varphi(t, z) \in Z \text{ for all } t \leq 0 \text{ and } \lim_{t \rightarrow -\infty} \varphi(t, z) = z_0 \right\},$$

respectively.

Important for our later applications will be the following theorem. It shows that for hyperbolic fixed points, one can always find an  $h$ -set  $N$  with cones in such a way that the unstable manifold  $W_N^u(z_0)$  is a horizontal disk in  $N$ , and that the stable manifold  $W_N^s(z_0)$  is a vertical disk.

**Theorem 3.8** (Invariant manifolds as disks [63, Theorem 26]). *Suppose that the point  $z_0$  is a hyperbolic fixed point for the ordinary differential equation (7). Moreover, let  $Z \subset \mathbb{R}^n$  denote an open set with  $z_0 \in Z$ . Then there exists an  $h$ -set  $N$  with cones such that the following hold:*

- We have both  $z_0 \in N$  and  $N \subset Z$ .
- The  $h$ -set  $N$  is an isolating block for the vector field  $f$ .
- The unstable manifold  $W_N^u(z_0)$  is a horizontal disk in  $N$  which satisfies the cone condition.
- The stable manifold  $W_N^s(z_0)$  is a vertical disk in  $N$  which also satisfies the cone condition.

Finally, the unstable manifold  $W_N^u(z_0)$  can be represented as the graph of a Lipschitz continuous function over the unstable space of the linearization of  $f$  at  $z_0$ , and this graph is tangent to the unstable space at  $z_0$ . An analogous statement holds for the stable manifold  $W_N^s(z_0)$ .

In our application below we are interested in a slightly different situation. In our case, the existence of the fixed point is not known ahead of time. Its existence is, however, a consequence of the existence of an isolating block. Such a theorem in the context of maps has been proven in [63, Theorem 10]. In the context of differential equations it has been first established in [33], see also [28, 62].

### 3.2 Self-consistent bounds

We now turn our attention to the concept of *self-consistent bounds*, which have been used extensively in recent years [14, 15, 28, 60, 61, 62, 64]. In the following, we recall the basic definitions and fundamental ideas behind this concept, and describe an application which will be used for our main result.

In its most general form, the method of self-consistent bounds applies to arbitrary *dissipative evolution equations* in a suitable subspace of the sequence space  $\ell^2$ , subject to certain admissibility conditions which depend on the specific notion of dissipativity. In other words, one can suppose that the underlying evolution equation takes the abstract form

$$\frac{du}{dt} = F(u), \quad (8)$$

where  $F$  is defined on a suitable subspace of  $\ell^2$  and takes values in the sequence space. Rather than presenting the concept of self-consistent bounds in this general setting, we right away specialize to the situation of the present paper. Our base space is the Hilbert space  $H' \subset \ell^2$  which was introduced in Definition 2.1, and we consider the infinite system of ordinary differential equations given by (5). In other words, in our situation the abstract equation (8) can be written in coordinate form as

$$\frac{da_k}{dt} = F_k(a) = \left( -\frac{k^4 \pi^4}{L^4} + \frac{\lambda k^2 \pi^2}{L^2} - \lambda \sigma \right) a_k - \frac{\lambda k^2 \pi^2}{L^2} \sum_{\substack{j_1, j_2, j_3 \in \mathbb{Z} \\ j_1 + j_2 + j_3 = k}} a_{j_1} a_{j_2} a_{j_3} \quad \text{for all } k \geq 0, \quad (9)$$

where  $a_0(t) \equiv 0$ . Without going into details, we note that the right-hand side is well-defined for all sequences  $a \in H'$ . In fact, the algebraic decay imposed through the subspace  $\tilde{H}$  in Definition 2.1 guarantees the four-time continuous differentiability of the function  $u$  given by (4), and therefore standard regularity results for parabolic partial differential equations ensure the well-posedness of (9) in the space  $H'$ .

The basic idea behind the method of self-consistent bounds is the construction of a suitable subset of the phase space of (8), in our case the Hilbert space  $H' \subset \ell^2$ , for which one can easily determine the flow across its boundary. Usually, such a set is constructed as an infinite product of intervals for each of the coefficients  $a_k$  of the sequences  $a \in H'$ , where, in order to be able to handle this set computationally, a bound for infinite number of them is provided by an algebraic decay. More precisely, let  $a_k^-$  and  $a_k^+$  denote the lower and upper bounds, respectively, for the  $k$ -th coefficient  $a_k$ , i.e., we will assume that elements of the constructed set satisfy  $a_k \in [a_k^-, a_k^+]$ , as long as  $k$  is sufficiently large. In detail, self-consistent bounds are defined as follows.

**Definition 3.9** (Self-consistent bounds). *Consider a set of the form*

$$W \oplus T = \{a \in H' \mid (a_1, \dots, a_m) \in W \text{ and } (a_{m+1}, a_{m+2}, \dots) \in T\} \subset H',$$

which is the product of a finite-dimensional set  $W \subset \mathbb{R}^m$  and an infinite-dimensional tail  $T \subset \mathbb{R}^\infty$ . Then the set  $W \oplus T$  forms self-consistent bounds for the evolution equation (9) if and only if the following conditions are satisfied.

- The infinite-dimensional tail  $T$  is given by an infinite product of intervals in the form

$$\mathbb{R}^\infty \supset T = \prod_{k>m} [a_k^-, a_k^+].$$

Moreover, there exists a usually large integer  $M > m$  such that  $a_k^- \leq 0 \leq a_k^+$  for all  $k \geq M$ , i.e., all but finitely many of the intervals in  $T$  contain zero.

- There exists a constant  $C > 0$  and an exponent  $s \geq 6$  such that  $|a_k^\pm| \leq C/|k|^s$  for all  $k \in \mathbb{N}$ .
- The vector field  $F$  points inwards on the parts of the boundary of  $W \oplus T$  which are associated with the components in the tail  $T$  in the sense that for all sequences  $x \in W \oplus T$  we have

$$F_k(x) > 0 \text{ if } x_k = a_k^-, \quad \text{and} \quad F_k(x) < 0 \text{ if } x_k = a_k^+, \quad \text{for all } k > m.$$

The evolution equation (9) represents a dissipative partial differential equation in the sense discussed in [60, 61, 64]. Moreover, one can show that the right-hand side operator in (9) is in fact continuous on the set  $W \oplus T$ . The *block decomposition* of the underlying Hilbert space  $H'$  is given by the infinite sum

$$H' = H'_1 \oplus H'_2 \oplus \dots, \tag{10}$$

where the subspace  $H'_k$  is the orthogonal projection onto the subspace of  $H'$  which corresponds to the  $k$ -th cosine basis vector via (4). For all of our considerations we will not use the standard induced norm on  $H'$ , but rather the so-called *block-infinity* norm given by

$$|x|_{b,\infty} := \max_{k \in \mathbb{N}} |x_k| \quad \text{for all } x = \{x_k\}_{k \in \mathbb{Z}} \in H',$$

This norm was introduced in [60]. For later applications, we also define the projection  $P_n: H' \rightarrow \mathbb{R}^n$  which maps  $a$  to  $(a_1, \dots, a_n)$  for all  $n \in \mathbb{N}$ . Finally, within the set of self-consistent bounds  $W \oplus T \subset H'$  for (9) we have

- uniform convergence and existence of a solution for the infinite-dimensional system (9),
- the solutions of (9) are uniquely determined, and
- one can derive a bound for the *Lipschitz constant* of the associated flow.

For more details on the justifications for each of these statements we refer the reader to [60].

### 3.3 Cone conditions in infinite dimensions

In this section we briefly describe how the finite-dimensional cone conditions from Section 3.1 can be interpreted in the infinite-dimensional self-consistent bounds setting. The involved results have appeared in two recent works on computer-assisted proofs for partial differential equations. On the one hand, they were used to establish a heteroclinic connection for the Kuramoto-Sivashinsky partial differential equation in [65]. In addition, in the recent thesis [36] they are fundamental for the computation of rigorous enclosures of unstable manifolds in the Cahn-Hilliard equation.

As a first step, we have to extend the notion of *h-set* to the infinite-dimensional self-consistent bounds setting. This can be accomplished as follows.

**Definition 3.10** (Self-consistent bounds and *h-sets*). *Suppose that  $W \oplus T \subset H'$  establishes self-consistent bounds for the evolution equation (9). Then the set  $W \oplus T$  is an *h-set*, if and only if the finite-dimensional part  $W$  is an *h-set* in the sense of Definition 3.1.*

Our primary interest is the verification of cone conditions for self-consistent bounds for the evolution equation (9) for the purposes of establishing the existence of an equilibrium solution in the self-consistent bound set, and to recognize the unstable manifold at this stationary state as a suitable horizontal disk. This is the subject of the next theorem, which states that if the cone condition has been verified for self-consistent bounds  $W \oplus T$  and a specific matrix  $Q$ , then there exists a stationary point  $z_0 \in W \oplus T$  for (9), and the unstable manifold  $W_N^u(z_0)$  is a horizontal disk in  $W \oplus T$  which satisfies the cone condition.

**Theorem 3.11** (Consequences of the cone condition). *Consider self-consistent bounds  $W \oplus T \subset H'$  for (9), and assume that the orthogonal projection  $P_n(W \oplus T)$  is an isolating block for the  $n$ -th Galerkin approximation (6) of (9) for all  $n > M$ . In addition, let  $Q$  denote an infinite diagonal matrix with  $Q_{jj} = 1$  for all indices  $j$  corresponding to the unstable directions and  $Q_{jj} = -1$  for the stable ones. Using this matrix, we assume that*

$$w^t \left( [dF(W)]^T Q + Q [dF(W)] \right) w > 0 \quad (11)$$

for all  $w \neq 0$  of the form  $w = x - y$ , where  $x, y \in W$ .

Then there exists an equilibrium  $z_0 \in W \oplus T$  for (9) and the unstable manifold  $W_N^u(z_0)$  is a horizontal disk in  $W \oplus T$  which satisfies the cone condition, where we set  $N = W \oplus T$ . Moreover, the manifold  $W_N^u(z_0)$  can be represented as the graph of a Lipschitz continuous function over the unstable space.

For a detailed proof we refer the reader to [36, 65]. Basically, this theorem follows from the finite-dimensional version given in Theorem 3.8, combined with the fact that within self-consistent bounds  $W \oplus T \subset H'$  both the Fourier series of all terms appearing in the right-hand side  $F$  of (9) and all partial derivatives in  $dF$  converge uniformly. This allows one to establish the existence of unstable manifolds for all Galerkin approximations of (9) with uniform bounds, which in addition are contained in a compact set. One can now employ a standard convergent subsequence argument to establish the existence of an unstable manifold for the infinite-dimensional system (9). Moreover, the verification of positive definiteness of the infinite-dimensional matrix  $[dF(W)]^T Q + Q [dF(W)]$  reduces

to the verification of positivity of a finite number of inequalities, due to the polynomial growth of the diagonal which stems from the quartic increase of the eigenvalues of the linear part of (9). Finally, since the equation is dissipative, for sufficiently large  $k$  the eigenvalues of the linear part of (9) are all negative, and therefore we have  $Q_{kk} = -1$  for all these indices. In order to verify (11), we make use of the following lemma.

**Lemma 3.12** (Verifying the cone condition). *If for some  $\varepsilon > 0$  and for all  $k \in \mathbb{N}$  one can show that*

$$2 \inf_{x \in W} \left| \frac{\partial F_k}{\partial x_k}(x) \right| - \sum_{\ell \neq k} \sup_{x \in V} \left| Q_{\ell\ell} \frac{\partial F_\ell}{\partial x_k}(x) + Q_{k\ell} \frac{\partial F_k}{\partial x_\ell}(x) \right| \geq \varepsilon, \quad (12)$$

*is satisfied, then the inequality (11) holds.*

It will be the subject of Section 6 below how this infinite-dimensional condition can be verified computationally, and this will provide the unstable equilibrium which forms the initial point for our heteroclinic solutions.

Finally, we would like to mention that the existence of a stable steady state of (9) can be accomplished by checking suitable estimates for *logarithmic norms*, which were introduced in [16, 27]. In addition, such logarithmic norm estimates will provide explicit bounds for the size of the basin of attraction of the stable steady state. For this, we basically apply the theory, algorithms, and code from [12, 14, 60], and the interested reader is referred to these papers for more details. We do not further describe the details this verification procedure, since the logarithmic norm condition is equivalent to the cone condition (12) with only stable directions, i.e., with the matrix  $Q$  being given by  $-\text{Id}$ , where  $\text{Id}$  denotes the infinite-dimensional identity matrix.

## 4 Proof of the main result

With this section we begin proving our main result, which was described in Theorem 1.1 in the introduction. While this result guarantees the existence of heteroclinic connections between an unstable index two stationary solution, which in fact is the homogeneous steady state, and two stable local energy minimizers, its formulation concentrated on the diblock copolymer model on the domain  $\Omega = (0, 1)$ . This choice was motivated by the studies in [24], yet for numerical reasons it is not optimal. In fact, by naively choosing the parameters as in Theorem 1.1 one ends up with an extremely stiff Galerkin approximation (6).

In order to overcome this stiffness problem, we make use of standard rescaling arguments. For this, assume that  $u$  denotes a solution of the diblock copolymer model (2) on the one-dimensional domain  $\Omega = (0, 1)$ , and for fixed parameters  $\lambda = 1/\varepsilon^2 > 0$  and  $\sigma > 0$ . Furthermore, let  $L > 0$  be a fixed interval length, and define a function  $v : \mathbb{R}_0^+ \times (0, L) \rightarrow \mathbb{R}$  via

$$v(\tau, y) = u \left( \frac{\lambda\tau}{L^4}, \frac{y}{L} \right) \quad \text{for all } \tau \geq 0 \quad \text{and} \quad y \in (0, L).$$

Then one can easily verify that  $v$  solves the diblock copolymer equation

$$v_\tau = - \left( v_{yy} + \frac{\lambda}{L^2} \cdot f(v) \right)_{yy} - \frac{\sigma}{L^2} \cdot \frac{\lambda}{L^2} \cdot (v - \mu) \quad \text{on the domain } \mathbb{R}_0^+ \times (0, L),$$

which is exactly of the form given in (3), but with rescaled parameters  $\lambda$  and  $\sigma$ .

It turns out that for the parameter combinations given in Theorem 1.1 it is most convenient to choose the new domain length  $L = 2\pi$ , since this reduces the size of the eigenvalues of the linearized Galerkin approximation (6). Thus, in the following, we will establish the following rescaled result.

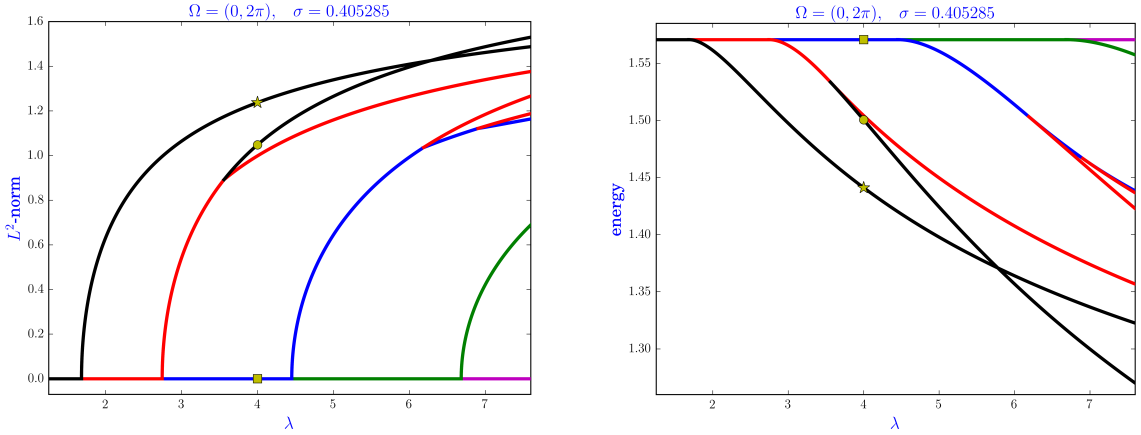


Figure 5: Bifurcation diagrams for the diblock copolymer model (2) on the (rescaled) domain  $\Omega = (0, 2\pi)$ , for total mass  $\mu = 0$ , and for nonlocal interaction parameter  $\sigma = 16/(2\pi)^2 \approx 0.405285$ . In the left diagram, the vertical axis measures the  $L^2(0, 2\pi)$ -norm of the solutions, while the right diagram shows the total energy (1). In both diagrams, the horizontal axis uses the parameter  $\lambda = 1/\epsilon^2$ . As in Figure 1, the solution branches are color-coded by the Morse index of the solutions, and black, red, blue, green, and magenta correspond to indices 0, 1, 2, 3, and 4, respectively.

**Theorem 4.1** (Rescaled version of the main theorem). *Consider the diblock copolymer equation (3) on the domain  $\Omega = (0, L)$  with  $L = 2\pi$ , for interaction lengths  $\lambda = 4$  and  $\sigma = 4/\pi^2 \approx 0.405284735$ , and for total mass  $\mu = 0$ . Then there exist heteroclinic connections between the unstable homogeneous stationary state  $u \equiv 0$ , which is indicated by a yellow square in Figure 5, and*

- (a) *Each of the two local energy minimizers which are indicated by yellow circles, as well as*
- (b) *Each of the two global energy minimizers which are indicated by yellow stars.*

*In other words, for the above parameter combinations, the diblock copolymer equation exhibits multistability, and all energy minimizers can be reached from any arbitrarily small neighborhood of the homogeneous state.*

To illustrate the formulation of the above theorem, we have included the bifurcation diagrams for the new, rescaled situation in Figure 5. Compare also their original counterparts in Figure 3.

Before turning our attention to the proof of Theorem 4.1, we need to introduce some notation. In the following, we denote the unstable homogeneous steady state of (3) at origin by  $z_0^u \in H'$ . This equilibrium is indicated by a yellow square in Figure 5. In addition, let  $z_0^{s,loc} \in H'$  denote one of the two stable local energy minimizers of (1), which are indicated by a yellow circle in Figure 5. Let  $z_0^{s,glob} \in H'$  denote one of the two global energy minimizers of (1), which are indicated by yellow star in Figure 5. One can easily see that the theorem only has to be verified for one of these local/global minima, the result for the second one follows from symmetry arguments.

For each of the involved equilibrium solutions, we need to construct self-consistent bounds containing them. Thus, we let

$$\mathcal{W}_s^{loc} \subset H'$$

denote the infinite-dimensional stable isolating block which contains the stable steady state  $z_0^{s,loc}$ , and which forms self-consistent bounds. We also let

$$\mathcal{W}_s^{glob} \subset H'$$

denote the infinite-dimensional stable isolating block which contains the stable steady state  $z_0^{s,glob}$

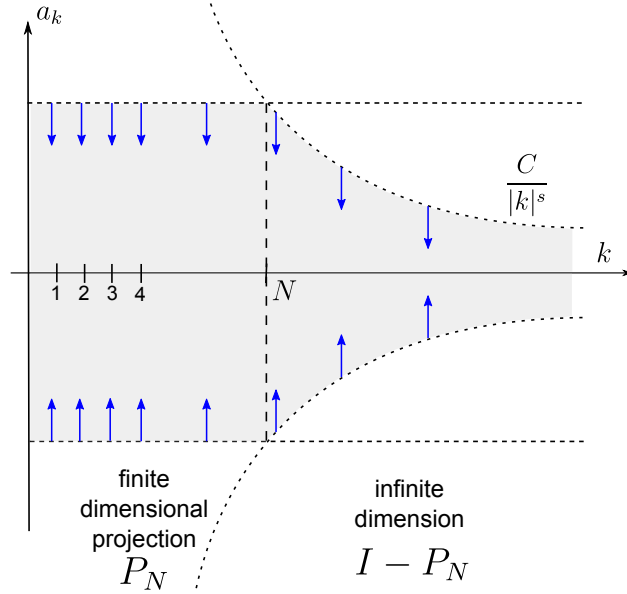


Figure 6: The stable isolating block  $\mathcal{W}_s^{loc}$  and its infinite-dimensional self-consistent bounds structure. The isolating block has the topological property that the vector field in (9) points inwards in all coordinate directions.

As long as it also satisfies the cone condition, the existence of stable steady states in  $\mathcal{W}_s^{loc}$  and  $\mathcal{W}_s^{glob}$  follows then from Theorem 3.11 with all directions being stable directions, as illustrated in Figure 6. Now consider the unstable equilibrium involved in the heteroclinic. Let

$$\mathcal{W}_u \subset H'$$

denote the infinite-dimensional unstable isolating block which contains the known unstable equilibrium  $z_0^u = 0$ , and which forms self-consistent bounds. In this case, if the block satisfies the cone condition, then the existence of a two-dimensional unstable manifold is guaranteed at the origin by Theorem 3.11, as is the fact that the manifold is a horizontal disk in  $\mathcal{W}_u$ . See also the illustration in Figure 7. After these preparations, we can now proceed with the proof of Theorem 4.1.

*Proof.* The verification of Theorem 4.1 is divided into three parts, which are described in more detail below. We would like to point out already now that all sets used in the proof are constructed using rigorous numerical programs which are based on *interval arithmetic*, see for example [35]. In this way, all computations done by a computer are validated in a strict mathematical sense. In particular, if the program verifies the cone condition for the whole set under consideration, this automatically implies that the condition is satisfied for all elements of this set. For more illustrations of this approach, also in other contexts, we refer the interested reader to [49].

**First step:** Using a computer program based on interval arithmetic, we first construct self-consistent bounds  $\mathcal{W}_u \subset H'$  in such a way that  $\mathcal{W}_u$  is an unstable isolating block for (9). For this, the set  $\mathcal{W}_u$  is centered at the origin, which represents our known unstable equilibrium  $z_0^u$  for (9). More specific information regarding the specific choice of  $\mathcal{W}_u$  is presented in Appendix A.1, which contains verified numerical data from the program. These results show that the topological structure of  $\mathcal{W}_u$  is exactly of the form shown in Figure 7. In addition, the set  $\mathcal{W}_u$  is verified to satisfy the cone condition (12). Now Theorem 3.11 implies that the unstable manifold  $W_N^u(z_0^u)$  is a horizontal disk in  $\mathcal{W}_u$ , and therefore the unstable manifold at the origin crosses one of the faces of  $\mathcal{W}_u$ . Let  $W_0$  denote such a face, see also the diagram in Figure 8. The whole construction of  $\mathcal{W}_u$  relies on the fact

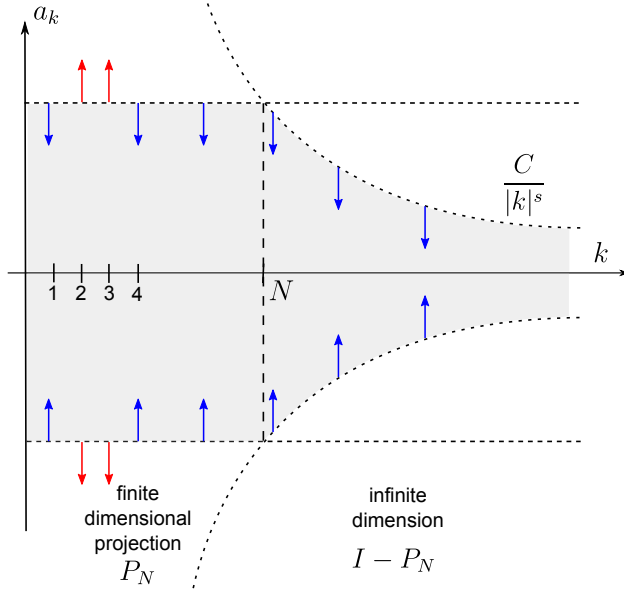


Figure 7: The unstable isolating block  $\mathcal{W}_u$  which contains the unstable homogeneous equilibrium of (3) at the origin, and its infinite-dimensional self-consistent bounds structure. This isolating block has the topological property that the vector field in (9) points outwards for the second and third coordinate directions, while pointing inwards for all remaining directions. Once the cone condition given in Lemma 3.12 has been verified for this block, the existence of a two-dimensional unstable manifold follows, as well as the fact that it is a horizontal disk within the depicted set.

that the unstable equilibrium  $z_0^u$  is given by the origin. We can therefore determine the eigenfunctions of the linearization of (9) at  $z_0^u$  explicitly, and this easily shows that all eigenfunctions are just the basis functions  $e_k(x)$  for  $k \in \mathbb{N}$ . Furthermore, recall from our brief discussion in the introduction that for our choice of  $\sigma$  the two unstable eigendirections correspond to the eigenfunctions  $e_2(x)$  and  $e_3(x)$ . In order to make the subsequent parts of the proof computationally faster, we stretch the set  $\mathcal{W}_u$  along the second eigenfunction, which is given by  $e_3(x)$  (we denote the face of  $\mathcal{W}_u$  in this direction by  $W_0(e_3)$ ) for the case of the connection to the local minimizer. We also stretch it along the third eigenfunction  $e_2(x)$  for the case of the global minimizer (we denote the face of  $\mathcal{W}_u$  in this direction by  $W_0(e_2)$ ). See again Figure 8.

**Second step:** Similar to the first step, we use interval arithmetic to construct self-consistent bounds  $\mathcal{W}_s^{loc}, \mathcal{W}_s^{glob} \subset H'$  in such a way that  $\mathcal{W}_s^{loc}, \mathcal{W}_s^{glob}$  is a stable isolating block for (9). The block  $\mathcal{W}_s^{loc}$  is centered at a numerically computed approximation to the actual stable equilibrium  $z_0^{s,loc}$ , and the topological structure of  $\mathcal{W}_s^{loc}$  is as indicated in Figure 6. Analogously, the block  $\mathcal{W}_s^{glob}$  is centered at a numerically computed approximation to the stable equilibrium  $z_0^{s,glob}$  – the global minimizer. The finite-dimensional part of this set is determined in an appropriate coordinate system, which is given by the numerically determined eigenbasis of the Jacobian matrix at the numerical approximation of  $z_0^{s,loc}, z_0^{s,glob}$  respectively. As a consequence, the block decomposition (10) of  $H'$  takes on the following form. The first  $m$  coordinates correspond to the eigenbasis of the  $m$ -th Galerkin approximation (6), while the remaining coordinate directions are given by the standard basis functions  $e_k(x)$  for  $k > m$ . In other words, we have to take into account that the Jacobian at  $z_0^{s,loc}, z_0^{s,glob}$  is considered in two different coordinate systems, and this is handled as outlined in more detail in [12, 60]. Next, the computer program is used to compute a verified upper bound on the logarithmic norm of the Jacobian in block coordinates (10). As can be seen from the numerical data in Appendix A.1, this bound turns out to be negative. Notice that determining an upper bound for a logarithmic norm is equivalent to

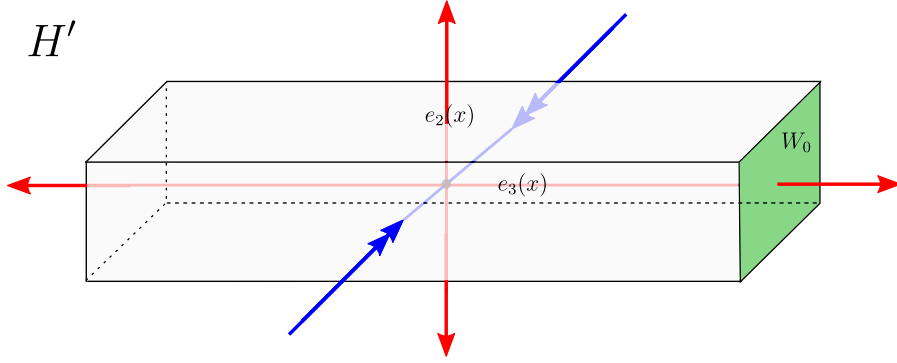


Figure 8: Sketch of the isolating block  $\mathcal{W}_u$  centered at the unstable equilibrium  $z_0^u$ , which is the homogeneous zero state. The eigenfunctions  $e_2(x)$  and  $e_3(x)$  correspond to the two unstable directions, as can be easily seen by determining the linearization of (9) at zero. For establishing the existence of the heteroclinic, the face  $W_0$  will be propagated forward in time through rigorous integration. We illustrate the unstable isolating block that we construct in the case of the connection to the local minimizer. For the case of the connection to the global minimizer it is stretched along  $e_2$  eigendirection instead of  $e_3$ .

computing the cone condition (12) in the situation of only stable directions, and our program makes use of the techniques described in more detail in [12, 60]. Thus, the numerical data presented in the appendix ensures the existence of an attracting equilibria for (9), namely  $z_0^{s,loc}$  in  $\mathcal{W}_s^{loc}$ , and  $z_0^{s,glob}$  in  $\mathcal{W}_s^{glob}$ . In addition, we obtain that the complete sets  $\mathcal{W}_s^{loc}$ ,  $\mathcal{W}_s^{glob}$  are contained in the basin of attraction of  $z_0^{s,loc}$ , and  $z_0^{s,glob}$  respectively.

**Third step:** Since the first two steps of the proof have established sets  $W_0(e_2), W_0(e_3)$  which contains part of the unstable manifold of  $z_0^u$ , as well as a subsets  $\mathcal{W}_s^{loc}$ ,  $\mathcal{W}_s^{glob}$  which are contained in the basin of attraction of  $z_0^{s,loc}$ ,  $z_0^{s,glob}$  respectively, it only remains to show that all solutions of (9) which originate in  $W_0(e_3)$  end up in  $\mathcal{W}_s^{loc}$ , and all solutions of (9) which originate in  $W_0(e_2)$  end up in  $\mathcal{W}_s^{glob}$ . This is accomplished in the last step of the proof through rigorous forward integration of the flow associated with (9). For this, we use the algorithm for rigorous integration described in the series of works [12, 25, 61, 64]. In fact, we make use of an optimized version of this algorithm which was developed in [11], and this version will be described in more detail in the next Section 5. In this way, we are able to rigorously propagate the sets  $W_0$  forward in time in such a way that all computational errors are accounted for, and we obtain that the flow of (9) in  $H'$  transports  $W_0(e_3)$  into  $\mathcal{W}_s^{loc}$ , and  $W_0(e_2)$  into  $\mathcal{W}_s^{glob}$ . A cartoon of this procedure is shown in Figure 9. In the figure, the sets  $[\Phi(kh, W_0)]$  denote rigorous enclosures for the images of  $W_0$  under the flow at time  $kh$ , for integers  $k > 0$ . After  $N + 1$  steps of this forward integration by time  $h$ , the final enclosure is shown to be contained in  $\mathcal{W}_s^{loc}$ , and therefore the basin of attraction of  $z_0^{s,loc}$ . In the actual computation performed by a computer program any initial condition in the face  $W_0(e_3)$  of  $\mathcal{W}_u$  at time  $T = 3.02$  (after performing 1510 numerical integration steps) is verified to be within  $\mathcal{W}_s^{loc}$ , and any initial condition in the face  $W_0(e_2)$  of  $\mathcal{W}_u$  at time  $T = 4.62$  (after performing 2310 numerical integration steps) is verified to be within  $\mathcal{W}_s^{glob}$ . As a consequence, one obtains the existence of a manifold  $W^u(z_0^u) \cap W^s(z_0^{s,loc})$  which connects the unstable equilibrium  $z_0^u$  with the stable equilibrium  $z_0^{s,loc}$ . As well as the existence of a manifold  $W^u(z_0^u) \cap W^s(z_0^{s,glob})$  which connects the unstable equilibrium  $z_0^u$  with the stable equilibrium  $z_0^{s,glob}$ . For more details on the numerical data from the actual computations we refer the reader to Appendix A.1 and the numerical data available in an online repository [13]. Needless to say, the third and last step of the proof is the most time consuming part.  $\square$

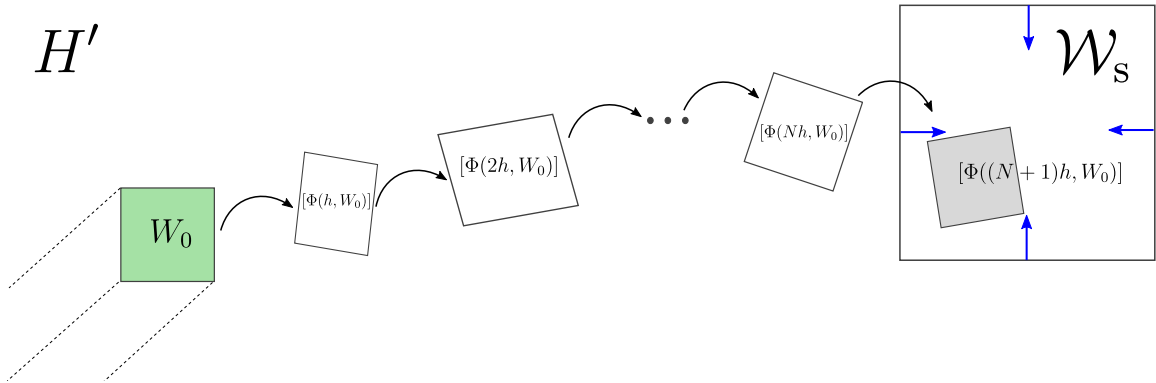


Figure 9: The last part of the proof described in Step 3 establishes the existence of a heteroclinic connection. This is accomplished through rigorous integration forward in time of the face  $W_0$  of  $\mathcal{W}_u$ , which was indicated in Figure 8. Notice that this numerical integration has to be performed for the infinite-dimensional system (9) with phase space  $H'$ .

We would like to close this section with a brief comment on the applicability of the above approach. The proof given above defines an algorithm for proving Theorem 4.1. The algorithm is general. While in the proof we have considered a very specific instance of the diblock copolymer model, for a particular set of parameters, in principle the algorithm applies to the verification of any saddle to sink connection for the diblock copolymer model (9). The algorithm describes numerical verification needed to be performed with a clear separation of the computation into three consecutive steps. We have implemented a computer program, realizing this algorithm, which is part of the publication [13] and available online. The input to the program are the parameters in the equation, and if the program terminates successfully we have proved the existence of a heteroclinic. The main prerequisite for termination is of course that the set propagated by the rigorous numerical integrator is mapped completely inside the stable isolating block  $\mathcal{W}_s^{loc}$ . However, the process of obtaining such a proof for arbitrary parameters is not fully automated. In general, one has to try to make the set  $\mathcal{W}_s^{loc}$  as large as possible, while at the same time keeping  $W_0$  small. In this way, the accumulated effect of roundoff errors and inherent expansion in the differential equation can often be controlled.

## 5 Rigorous integration algorithm

To rigorously integrate (9) forward in time we apply an algorithm based on the rigorous *Taylor method*, as well as the *Lohner algorithm* for an efficient representation of sets and to avoid the *wrapping effect*. The Lohner algorithm is presented in detail in [25, 26]. We specifically use the algorithm introduced in [11], which allows for the efficient implementation of the Taylor method for differential equations in combination with the variational equations arising in partial differential equations. This algorithm combines *automatic differentiation* with the *fast Fourier transform algorithm*. In the remainder of this section, we briefly explain the ideas behind this algorithm, and discuss why it is much more efficient than the direct method of computation of normalized derivatives. For a more detailed discussion, we refer the reader to [11], where a computational complexity analysis can be found in the context of partial differential equations with a quadratic nonlinearity. We will demonstrate below that this analysis can be extended to the diblock copolymer model (3) with a cubic nonlinearity. In fact, in the situation of the present paper, the method of [11] leads to even greater speedups. One of the main advantages of the method of [11] is that it allows one to use a high-order Taylor method as opposed to the direct integration method. In fact, in the actual proof of the results of this paper we use a Taylor method of order 16.

To describe our approach in more detail, consider again the right-hand side  $F$  of (9). In addition, we denote the right-hand side of the  $m$ -th Galerkin approximation (6) by  $F_m$ . We begin by giving a brief description of how the actual solution of an initial value problem for (9) can be enclosed in an efficient way. This is achieved by bounding the solution set of the *differential inclusion* given by

$$\frac{dz}{dt}(t) \in F_m(z(t)) + [\delta], \quad (13)$$

where  $z(t)$  takes values in  $\mathbb{R}^m$ . More precisely, the solution set of (13) is bounded by first enclosing the solution of the *Cauchy problem* associated with (13), and then adding appropriate *a-posteriori* bounds, see for example [12, 25] for more details.

In order to rigorously enclose the solution of the Cauchy problem associated with (13), we make use of the classical Taylor method. Thus, the enclosure for the solution is propagated by one time step through the knowledge of the *normalized derivatives* of orders up to  $p$ , where the integer  $p$  denotes the order of the Taylor method. These normalized derivatives are defined as follows.

**Definition 5.1** (Normalized derivative). *Let  $n > 0$  be an arbitrary integer, and let  $w: [0, t_{max}) \rightarrow \mathbb{R}$  denote a sufficiently smooth function. Then the  $n$ -th normalized derivative of  $w$  is defined as*

$$w^{[n]}(t) = \frac{1}{n!} w^{(n)}(t),$$

where  $w^{(n)}(t)$  denotes the classical  $n$ -th derivative of  $w$ .

According to this definition, the normalized derivatives are precisely the terms occurring in a standard Taylor expansion. They can be determined efficiently via a well-known recursive formula from *automatic differentiation*, which is recalled in the next remark.

**Remark 5.2** (Recursion for normalized derivatives). *For an ordinary differential equation of the form*

$$\frac{dz}{dt} = G(z), \quad \text{where } z \in \mathbb{R}^m, \quad \text{and } G: \mathbb{R}^m \rightarrow \mathbb{R}^m,$$

the normalized derivatives of  $z$  can be determined as follows. If we set  $z^{[0]} = z^{(0)}$ , then for arbitrary differentiation orders  $j = 1, \dots, q-1$  the normalized derivative  $z^{[j]}$  is given by the recursive formula

$$z^{[j+1]} = \frac{1}{j+1} (G \circ z)^{[j]},$$

as long as  $G$  is  $q$ -times differentiable.

After these preparations we can now analyze the cost of computing the  $(p+1)$ -st order Taylor method for the finite system of ordinary differential equations given by the Galerkin approximation (6). If we assume that the normalized derivatives of  $u$  of orders  $1, 2, \dots, p$  have already been computed, then the cost of determining the  $(p+1)$ -st normalized derivative is equivalent to the cost of evaluating the convolutions

$$(u * u * u)_k^{[p]} \quad \text{for all indices } |k| \leq m,$$

where the function  $u$  is given by its time-dependent Fourier coefficients, and  $[p]$  denotes  $p$ -th normalized derivative with respect to time.

Since we are interested in using the Lohner algorithm [26], we not only have to keep track of the Fourier coefficients of the solution  $u$ , but also of the associated derivatives vector, which is usually referred to as the *jet*. Thus, in order to emphasize this fact we will from now on write  $\mathbf{u}$  instead of  $u$ , and our goal is the computation of the convolutions

$$(\mathbf{u} * \mathbf{u} * \mathbf{u})_k^{[p]} \quad \text{for all indices } |k| \leq m,$$

which can be expanded as

$$(\mathbf{u} * \mathbf{u} * \mathbf{u})_k^{[p]} = \sum_{\substack{0 \leq p_1, p_2, p_3 \leq p \\ p_1 + p_2 + p_3 = p}} \sum_{\substack{|k_1|, |k_2|, |k_3| \leq m \\ k_1 + k_2 + k_3 = k}} \mathbf{u}_{k_1}^{[p_1]} \mathbf{u}_{k_2}^{[p_2]} \mathbf{u}_{k_3}^{[p_3]} \quad \text{for all } |k| \leq m. \quad (14)$$

If we now let  $N$  denote the number of coefficients that are calculated in (14), along with their partial derivatives for the variational equations, then one can easily see that we basically have

$$N = m^2 + m,$$

up to a constant, which has to be large enough to avoid the *aliasing effect* (in our algorithm the constant is equal to 2). With this, one can finally analyze the computational cost of evaluating (14). While we do not present the details, the result is collected in the following remark.

**Remark 5.3** (Computational cost of evaluating the convolution). *The total cost of the direct evaluation of the convolution given in (14) is proportional to  $p^2 N^3$ , where  $N = m^2 + m$  up to a constant.*

Besides the above direct computation, it is well-known that one can evaluate convolutions as in (14) indirectly through the use of the *fast Fourier transform algorithm*. If we assume again that all normalized derivatives of  $u$  of order  $1, 2, \dots, p$  have already been computed, then the discrete functional values of the normalized derivatives of  $u$ , which are also called the *L-coefficients* in [11], have already been determined, and they can therefore be cached in memory. We denote these values by

$$\hat{\mathbf{u}}_j^{[r]} = \text{FFT}_j(\mathbf{u}^{[r]}) \quad \text{for all } r = 0, \dots, p, \quad j = 0, \dots, c \cdot m,$$

where  $\text{FFT}_j(\cdot)$  denotes the  $j$ -th component of the discrete Fourier transform computed by the fast Fourier transform method, and the constant  $c$  is specified below. Using these values, one can then determine (14) by computing the convolution for the *L-coefficients* in the form

$$\left(\widehat{\mathbf{u}^3}\right)_j^{[p]} = \sum_{\substack{0 \leq p_1, p_2, p_3 \leq p \\ p_1 + p_2 + p_3 = p}} \hat{\mathbf{u}}_j^{[p_1]} * \hat{\mathbf{u}}_j^{[p_2]} * \hat{\mathbf{u}}_j^{[p_3]} \quad \text{for all } j = 0, \dots, c \cdot m, \quad (15)$$

and then applying the inverse fast Fourier transform, which we denote by  $\text{FFT}^{-1}$ , in order to obtain

$$\left(\mathbf{u}^3\right)_k^{[p]} = \text{FFT}_k^{-1} \left( \left(\widehat{\mathbf{u}^3}\right)_k^{[p]} \right) \quad \text{for all } |k| \leq N. \quad (16)$$

After this, we can also calculate the *L-coefficients* of  $\hat{\mathbf{u}}^{[p+1]}$  and cache them in memory, provided we intend to increase the order further, i.e., we evaluate

$$\hat{\mathbf{u}}^{[p+1]} = \text{FFT}(\mathbf{u}^{[p+1]}).$$

While at first glance the approach based on the fast Fourier transform seems to be more involved, its computational savings are significant. To see this, recall that the cost of performing a fast Fourier transform is of the order  $N \log N$ , and therefore the same is true for the computation of (16). Moreover, the cost of computing the convolution for the *L-coefficients* (15) is just the cost of multiplying  $p^2 c N$  values, and this leads to the following observation.

**Remark 5.4** (Computational cost of the convolution via the fast Fourier transform). *If we assume that the *L-coefficients* of  $\hat{\mathbf{u}}$  have already been computed and cached in memory, then the total cost of the fast Fourier transform approach to the computation of (14) is proportional to*

$$\underbrace{N \log N}_{\text{dominant}} + p^2 c N. \quad (17)$$

Typically, the integer  $N$  is significantly larger than the order  $p$ , since it counts the number of equations and variational. Thus, in contrast to the formula given in Remark 5.3, the dominating cost term in (17) is given by  $N \log N$ . This implies that increasing the order  $p$  does not result in a severe increase of the total cost. The typical choice of the constant  $c$  in the above discussion is  $c = 3$ . Using some optimizations that were described in [11], one can in fact reduce the constant to  $c = 2$ .

Needless to say, in practice the fast Fourier transform technique greatly reduces the total running time of our computer-assisted proof.

**Remark 5.5.** *The actual running time of the integration step of the proof with parameters as reported in Appendix A.1 is triple reduced. The real time of the integration procedure on a laptop is 3m55s FFT vs 11m55 direct (without FFT) in case of the connection to the local minimizer, and 6m34s FFT vs 17m29s in case of the connection to the global minimizer.*

*We remark that the actual proof was performed with a moderate Galerkin approximation dimension ( $m = 15$ ), which allows to achieve the proof in a reasonable time on a laptop. In particular performing of an analogous proof, but for a parameter regime further from zero will require larger approximations, due to much more complicated dynamics on the attractor. The analysis of the algorithm presented in this section shows that for larger approximation dimension even a higher speedup is anticipated.*

## 6 Verifying the cone condition in infinite dimensions

This section is devoted to illustrating how the cone condition (12) can be verified in infinite dimensions. For the sake of brevity, this will only be done in the context of the set  $\mathcal{W}_u$ . As mentioned earlier, the verification of the cone condition for the remaining set  $\mathcal{W}_s^{loc}$  basically amounts to obtaining logarithmic norm estimates, and this can be achieved directly with the algorithms from [12, 60], and is therefore omitted in the following. To begin with, we would like to remind the reader that according to (12), we have to verify the estimate

$$2 \inf_{x \in \mathcal{W}_u} \left| \frac{\partial F_k}{\partial x_k}(x) \right| - \sum_{\substack{\ell \in \mathbb{Z} \\ \ell \neq k}} \sup_{x \in \mathcal{W}_u} \left| Q_{\ell\ell} \frac{\partial F_\ell}{\partial x_k}(x) + Q_{k\ell} \frac{\partial F_k}{\partial x_\ell}(x) \right| \geq \varepsilon, \quad (18)$$

for the unstable isolating block  $\mathcal{W}_u$ , for some  $\varepsilon > 0$  and for all  $k \in \mathbb{N}$ .

In order to accomplish this, the block  $\mathcal{W}_u \subset H'$  is divided into two parts, and we refer to this representation again as self-consistent bounds. More precisely, we have that

- the *finite part* for  $k = 1, \dots, M$  is represented as a finite-dimensional interval product, i.e., the projection  $(\mathcal{W}_u)_k$  is an interval, and
- the *tail*, which corresponds to  $k = M + 1, \dots$ , is represented by an algebraically decaying bound, i.e., for all  $x \in (\mathcal{W}_u)_k$  the inequality  $|x| \leq C/|k|^6$  is satisfied. In order to explicitly relate the constant  $C$  to the block  $\mathcal{W}_u$ , we will use the notation  $C(\mathcal{W}_u)$  in the following.

Notice that due to the inclusion  $\mathcal{W}_u \subset H'$ , the tail in the algorithm is represented by only the value of the constant  $C > 0$ .

In order to establish the cone condition, we first determine self-consistent bounds  $\mathcal{C} \subset H'$ , which bound all possible convolutions of elements from the block  $\mathcal{W}_u$ , i.e., such that for all  $k = 0, \dots, M$  we have

$$\mathcal{C}_k \quad \text{is such that} \quad \mathcal{C}_k \supset (a * b)_k \quad \text{for all} \quad a, b \in \mathcal{W}_u.$$

Since the nonlinearity in (9) is cubic, one therefore immediately obtains an enclosure for the partial derivatives matrix  $DF$  in the form

$$(DF)_{k\ell} = \frac{\partial F_k}{\partial x_\ell}(x) \subset \delta_{k\ell} \left( -\frac{k^4 \pi^4}{L^4} + \frac{\lambda k^2 \pi^2}{L^2} - \lambda \sigma \right) - \frac{3\lambda k^2 \pi^2}{L^2} (\mathcal{C}_{k-\ell} + \mathcal{C}_{k+\ell}) \quad \text{for all} \quad x \in \mathcal{W}_u.$$

Before proceeding, we need to introduce some notation. if  $I \subset \mathbb{R}$  denotes an arbitrary interval, then we denote the maximal absolute value of all points from  $I$  by  $|I|_{\max}$ . We can now estimate the second expression in (18) by

$$\sum_{\substack{\ell \in \mathbb{Z} \\ \ell \neq k}} \sup_{x \in \mathcal{W}_u} \left| Q_{\ell\ell} \frac{\partial F_\ell}{\partial x_k}(x) + Q_{kk} \frac{\partial F_k}{\partial x_\ell}(x) \right| \leq \frac{3\lambda\pi^2}{L^2} \sum_{\substack{\ell \in \mathbb{Z} \\ \ell \neq k}} \left| \ell^2 Q_{\ell\ell} (\mathcal{C}_{\ell-k} + \mathcal{C}_{k+\ell}) + k^2 Q_{kk} (\mathcal{C}_{k-\ell} + \mathcal{C}_{k+\ell}) \right|_{\max}.$$

The right-hand side in this estimate can be bounded further. For this, we split it into two parts to obtain

$$\begin{aligned} \frac{3\lambda\pi^2}{L^2} \sum_{\substack{\ell \in \mathbb{Z} \\ \ell \neq k}} \left| \ell^2 Q_{\ell\ell} (\mathcal{C}_{\ell-k} + \mathcal{C}_{k+\ell}) + k^2 Q_{kk} (\mathcal{C}_{k-\ell} + \mathcal{C}_{k+\ell}) \right|_{\max} = \\ \frac{3\lambda\pi^2}{L^2} \sum_{\substack{|\ell| \leq M+k \\ \ell \neq k}} \left| \ell^2 Q_{\ell\ell} (\mathcal{C}_{\ell-k} + \mathcal{C}_{k+\ell}) + k^2 Q_{kk} (\mathcal{C}_{k-\ell} + \mathcal{C}_{k+\ell}) \right|_{\max} + \\ \frac{3\lambda\pi^2}{L^2} \sum_{\substack{|\ell| > M+k \\ \ell \neq k}} \left| \ell^2 Q_{\ell\ell} (\mathcal{C}_{\ell-k} + \mathcal{C}_{k+\ell}) + k^2 Q_{kk} (\mathcal{C}_{k-\ell} + \mathcal{C}_{k+\ell}) \right|_{\max}. \end{aligned}$$

The first part of this sum consists of expressions which contain at least one term from the finite part. In addition, the first summand is a finite sum, and we can therefore compute it term by term using interval arithmetic. In contrast, the second summand is infinite and consists exclusively of terms from the tail part, which can therefore be estimated. Using standard results from rigorous numerics for partial differential equations this finally yields the estimate

$$\begin{aligned} \frac{3\lambda\pi^2}{L^2} \sum_{\substack{|\ell| > M+k \\ \ell \neq k}} \left| \ell^2 Q_{\ell\ell} (\mathcal{C}_{\ell-k} + \mathcal{C}_{k+\ell}) + k^2 Q_{kk} (\mathcal{C}_{k-\ell} + \mathcal{C}_{k+\ell}) \right|_{\max} \leq \\ \frac{3\lambda\pi^2}{L^2} \sum_{\substack{|\ell| > M+k \\ \ell \neq k}} \left| \ell^2 (\mathcal{C}_{\ell-k} + \mathcal{C}_{k+\ell}) \right|_{\max} + \frac{3\lambda\pi^2}{L^2} \sum_{\substack{|\ell| > M+k \\ \ell \neq k}} \left| k^2 (\mathcal{C}_{k-\ell} + \mathcal{C}_{k+\ell}) \right|_{\max} \leq \\ \frac{3\lambda\pi^2}{L^2} \left( \frac{2C(\mathcal{C})k^2}{5M^5} + \frac{2C(\mathcal{C})}{3M^3} (1 + k/M) \right), \end{aligned}$$

whose right-hand side is given explicitly — and from this one can easily establish the validity of (18), and therefore the cone condition.

## 7 Software

The computer program performing all computational steps required to prove Theorem 4.1, as described in more detail in the respective proof in Section 4, has been written in the C++ programming language. The source codes, some compiled binary files, and the numerical output from the actual proofs are available in an online bitbucket repository [13]. The published source codes for this work utilizes some parts of the rigorous numerics software package developed by the first author, which was dedicated to the study of dissipative partial differential equations based on Fourier series expansions. This package has been used in a number of different contexts as well, see for example [11, 12, 14].

The software package is written in such a way that it should be easily adaptable to other situations as well. More precisely, by performing only small modifications in the code, it can be applied to a

range of dissipative partial differential equations which are written in terms of infinite Fourier series. Examples include the viscous Burgers equation, the Kuramoto-Sivashinsky equation, and the Swift-Hohenberg equation. The main part of the software package is a dedicated algorithm for performing time integration using Taylor’s method, and the efficient computation of the (higher order) time derivatives of the flow. The latter are required by Taylor’s method, and they are determined using the FFT algorithm described earlier.

## 8 Conclusion and future work

In this paper, we have presented a first instance in which heteroclinic solutions can be rigorously determined for the diblock copolymer model on one-dimensional domains. Moreover, our results have shown that the model exhibits strong multistability in the sense that all (local or global) energy minimizers can be reached from arbitrarily small neighborhoods of the homogeneous steady state. In the near future we plan to extend the presented research to prove heteroclinic connections for a wide range of other parameter regimes, with particular emphasis on regions further from the homogeneous steady state. Moreover, we plan to perform similar studies on simple two-dimensional domains. Another intriguing possibility for future work is to apply the parametrization method [5] in the first step of the proof of Theorem 4.1. Recently, the parametrization method has been generalized to allow for the validation of unstable manifolds for parabolic partial differential equations, see for example [39, 51]. Using the parametrization method, bounds for the unstable manifold are obtained by computing its expansion in the form of a finite Taylor polynomial. In contrast, in the present work, we obtain bounds for the unstable manifold by verifying the cone condition on a linear segment. For nonlinear partial differential equations and nontrivial parameter values, it is expected that the unstable manifold behaves linearly only very close to the unstable steady state. We are convinced that, using the parametrization method, especially for high Taylor orders, one can compute bounds for the unstable manifold of the diblock copolymer model that reach much further than those obtained using a linear block and cone conditions. This in turn is expected to greatly reduce the work needed for performing the final step of the proof, i.e., using the rigorous integrator to demonstrate that the unstable manifold enters the basin of attraction of the stable steady state. This should make it possible to then establish a result analogous to Theorem 4.1, but for large parameter values.

## 9 Acknowledgments

The presented work was performed while the first author held post-doctoral positions at the Warsaw Center of Mathematics and Computer Science, Poland, and subsequently at Rutgers, The State University of New Jersey, USA. The idea for the study arose during the workshop “Rigorous computation for infinite-dimensional nonlinear dynamics” at the American Institute of Mathematics in Palo Alto, California, in August 2013. The work of the second author was partially supported by NSF grants DMS-1114923 and DMS-1407087.

## A Numerical data from the computer proof

### A.1 Heteroclinic to the local minimizer

In this appendix we present some numerical data from the computer-assisted part of the proof presented in this paper. For the sake of brevity we list only a small number of the relevant modes which are involved in the constructed infinite-dimensional bounds. In addition, only three decimals of all numerical values are shown. Complete and detailed numerical data presented with larger precision can be found online [http://bitbucket.org/dzako/dbcp\\_proof](http://bitbucket.org/dzako/dbcp_proof).

**Unstable isolating block  $\mathcal{W}_u \subset H'$  around zero.** This is the first step of the proof of the main theorem from Section 4. We mark with text in bold the numerical values for the eigendirection  $e_3$  along which the unstable manifold of the homogeneous state connects to the stable *local* minimizer ( $\mathcal{W}_u$  is stretched along this direction)..

<b>k</b>	<b><math>\mathbf{a}_k</math> interval in the form center + radius</b>
1	$0 + [-2.365, 2.365]10^{-16}$
2	$0 + [-1, 1]10^{-12}$
<b>3</b>	<b><math>[-0.075, 0.075]</math></b>
4	$0 + [-1.538, 1.538]10^{-15}$
5	$0 + [-3.038, 3.038]10^{-16}$
6	$0 + [-1.478, 1.478]10^{-16}$
7	$0 + [-9.664, 9.664]10^{-17}$
8	$0 + [-5.623, 5.623]10^{-17}$
9	$0 + [-5.193, 5.193]10^{-17}$
10	$0 + [-3.771, 3.771]10^{-17}$
11	$0 + [-3.332, 3.332]10^{-17}$
12	$0 + [-2.248, 2.248]10^{-17}$
13	$0 + [-2.33, 2.33]10^{-17}$
14	$0 + [-1.926, 1.926]10^{-17}$
15	$0 + [-1.69, 1.69]10^{-17}$
16 – 75	small intervals of width $\leq 10^{-20}$
$\geq 76$	$< 1.393 \cdot 10^{-46}/k^6$

The infinite-dimensional cone condition (18) is satisfied with

$$\varepsilon = 0.08478.$$

The file *unstable\_box\_log.txt* which can be found online [13] contains more detailed numerical data related to this computation. The actual running time of the program computing this set is negligible compared to the last step, i.e., the numerical integration. Therefore, we do not report it.

**Stable isolating block  $\mathcal{W}_s^{loc} \subset H'$**  This is the second step of the proof of the main theorem from Section 4. The block  $\mathcal{W}_s^{loc}$  is centered at a numerically computed approximation to the actual stable equilibrium  $z_0^{s,loc}$  which was loaded from the provided file *fixedPoint.in*.

<b>k</b>	<b>a<sub>k</sub></b>		
1	$3.321 \cdot 10^{-18} + [-6.895, 6.895]10^{-6}$	24	$-1.441 \cdot 10^{-17} + [-1.763, 1.763]10^{-7}$
2	$8.18 \cdot 10^{-17} + [-1.691, 1.691]10^{-4}$	25	$2.333 \cdot 10^{-20} + [-1.87, 1.87]10^{-7}$
<b>3</b>	<b><math>0.2956 + [-1.031, 1.031]10^{-5}</math></b>	26	$2.084 \cdot 10^{-20} + [-1.651, 1.651]10^{-7}$
4	$-6.551 \cdot 10^{-17} + [-9.807, 9.807]10^{-5}$	27	$3.847 \cdot 10^{-8} + [-7.323, 7.323]10^{-8}$
5	$-1.241 \cdot 10^{-17} + [-9.732, 9.732]10^{-6}$	28	$1.265 \cdot 10^{-20} + [-1.417, 1.417]10^{-7}$
6	$-1.411 \cdot 10^{-16} + [-2.994, 2.994]10^{-6}$	29	$1.257 \cdot 10^{-20} + [-1.366, 1.366]10^{-7}$
7	$-3.635 \cdot 10^{-18} + [-2.875, 2.875]10^{-6}$	30	$3.047 \cdot 10^{-16} + [-1.1, 1.1]10^{-7}$
8	$-9.215 \cdot 10^{-18} + [-1.417, 1.417]10^{-5}$	31	$7.491 \cdot 10^{-19} + [-1.754, 1.754]10^{-7}$
9	$-5.613 \cdot 10^{-3} + [-1.518, 1.518]10^{-6}$	32	$6.881 \cdot 10^{-19} + [-1.7, 1.7]10^{-7}$
10	$-2.005 \cdot 10^{-18} + [-6.141, 6.141]10^{-6}$	33	$-7.323 \cdot 10^{-10} + [-8.918, 8.918]10^{-8}$
11	$-4.048 \cdot 10^{-18} + [-1.659, 1.659]10^{-6}$	34	$7.818 \cdot 10^{-19} + [-8.435, 8.435]10^{-8}$
12	$4.056 \cdot 10^{-16} + [-1.001, 1.001]10^{-6}$	35	$7.079 \cdot 10^{-19} + [-1, 1]10^{-7}$
13	$-2.184 \cdot 10^{-18} + [-1.367, 1.367]10^{-6}$	36	$2.828 \cdot 10^{-16} + [-5.943, 5.943]10^{-8}$
14	$-1.914 \cdot 10^{-18} + [-1.559, 1.559]10^{-6}$	37	$7.42 \cdot 10^{-19} + [-1.151, 1.151]10^{-7}$
15	$1.062 \cdot 10^{-4} + [-6.264, 6.264]10^{-7}$	38	$6.551 \cdot 10^{-19} + [-1.099, 1.099]10^{-7}$
16	$-1.771 \cdot 10^{-19} + [-7.908, 7.908]10^{-7}$	39	$1.394 \cdot 10^{-11} + [-8.788, 8.788]10^{-8}$
17	$-1.616 \cdot 10^{-19} + [-5.853, 5.853]10^{-7}$	40	$-1.015 \cdot 10^{-12} + [-2.472, 2.472]10^{-10}$
18	$1.351 \cdot 10^{-16} + [-2.593, 2.593]10^{-7}$	41	$-1.129 \cdot 10^{-12} + [-2.747, 2.747]10^{-10}$
19	$-2.224 \cdot 10^{-19} + [-3.73, 3.73]10^{-7}$	42	$-6.509 \cdot 10^{-13} + [-1.584, 1.584]10^{-10}$
20	$-1.555 \cdot 10^{-19} + [-2.83, 2.83]10^{-7}$	43	$-1.184 \cdot 10^{-12} + [-2.881, 2.881]10^{-10}$
21	$-2.021 \cdot 10^{-6} + [-2.355, 2.355]10^{-7}$	44	$-1.08 \cdot 10^{-12} + [-2.627, 2.627]10^{-10}$
22	$6.774 \cdot 10^{-20} + [-3.8, 3.8]10^{-7}$	45	$-1.075 \cdot 10^{-12} + [-1.967, 1.967]10^{-10}$
23	$6.011 \cdot 10^{-20} + [-3.309, 3.309]10^{-7}$	46 – 250	small intervals of width $\leq 10^{-11}$
		$\geq 251$	$< 6.947 \cdot 10^{-38}/k^6$

The infinite-dimensional cone condition (18) is satisfied with

$$\varepsilon = 0.03816 ,$$

which equivalently means that the logarithmic norm estimate is strictly negative. The interval radii of the first 39 modes, separated above by a horizontal line, of the block  $\mathcal{W}_s^{loc}$  are given in the eigenbasis of the finite-dimensional derivative at  $z_0^{s,loc}$ . These coordinates are being written by the program into the file *Q.in*. The actual running time of the program computing this set is again negligible compared to the last step, i.e., the numerical integration. As before, we therefore do not report it.

The file *stable\_box\_log.txt* that can be found online [13] contains more detailed numerical data related with this computation.

**Result of the numerical integration.** This is the third and final step of the proof of the main theorem from Section 4. Some technical parameters of the numerical integration are chosen in the following way:

- The Taylor method order is 16,
- the constant time step is 0.002,
- the Galerkin projection dimension  $m$  is 15, the dimension used by the FFT-algorithm  $N$  is 32, see also the description in Section 5.
- The whole integration process took **3m55s** on an Intel®Core™i7-4610M CPU @ 3.00GHz x 4, compiled with gcc version 4.9.2 (64-bit Ubuntu 4.9.2-10ubuntu13) and with flags -O2 -frounding-math.
- In contrast, if instead of the FFT-algorithm we used the direct algorithm, then the whole integration process took **11m55s**.

The file *num\_integration\_log.txt* that can be found online [13] contains more detailed numerical data related to this computation. Specifically, the file contains

- the vector which is the finite-dimensional part of the propagated polynomial bounds, saved at each step of the integration,
- each 100 steps of the integration the full infinite-dimensional polynomial bounds,
- at each step of the integration information at which coordinates the entry of  $\mathcal{W}_0$  into  $\mathcal{W}_s^{loc}$  has not yet been attained.

The infinite-dimensional bounds at time  $T = 3.02$  after performing 1510 numerical integration steps are

<b>k</b>	<b>a<sub>k</sub></b>
1	$-1.014 \cdot 10^{-8} + [-1.49, 1.49]10^{-7}$
2	$1.454 \cdot 10^{-7} + [-2.748, 2.748]10^{-7}$
<b>3</b>	<b><math>0.2956 + [-8.522, 8.522]10^{-9}</math></b>
4	$-1.293 \cdot 10^{-7} + [-1.183, 1.183]10^{-7}$
5	$-7.29 \cdot 10^{-9} + [-3.619, 3.619]10^{-8}$
6	$-1.589 \cdot 10^{-11} + [-1.156, 1.156]10^{-9}$
7	$-3.299 \cdot 10^{-8} + [-1.501, 1.501]10^{-8}$
8	$1.725 \cdot 10^{-8} + [-2.031, 2.031]10^{-8}$
9	$-5.613 \cdot 10^{-3} + [-1.14, 1.14]10^{-9}$
10	$7.704 \cdot 10^{-9} + [-8.354, 8.354]10^{-9}$
11	$-7.297 \cdot 10^{-10} + [-4.831, 4.831]10^{-9}$
12	$1.083 \cdot 10^{-8} + [-4.586, 4.586]10^{-9}$
13	$5.124 \cdot 10^{-9} + [-7.282, 7.282]10^{-10}$
14	$1.396 \cdot 10^{-9} + [-9.208, 9.208]10^{-10}$
15	$1.063 \cdot 10^{-4} + [-4.66, 4.66]10^{-9}$
16	$-1.778 \cdot 10^{-10} + [-2.702, 2.702]10^{-10}$
17	$6.718 \cdot 10^{-12} + [-8.894, 8.894]10^{-11}$
18	$-8.661 \cdot 10^{-11} + [-1.11, 1.11]10^{-10}$
19	$-4.31 \cdot 10^{-11} + [-5.222, 5.222]10^{-11}$
20	$-5.023 \cdot 10^{-12} + [-3.588, 3.588]10^{-11}$
21	$-2.021 \cdot 10^{-6} + [-4.376, 4.376]10^{-10}$
22	$4.655 \cdot 10^{-12} + [-7.155, 7.155]10^{-12}$
23	$-2.128 \cdot 10^{-13} + [-2.362, 2.362]10^{-12}$
24	$2.481 \cdot 10^{-12} + [-3.129, 3.129]10^{-12}$
25	$1.17 \cdot 10^{-12} + [-1.405, 1.405]10^{-12}$
26	$1.492 \cdot 10^{-13} + [-9.22, 9.22]10^{-13}$
27	$3.847 \cdot 10^{-8} + [-1.241, 1.241]10^{-11}$
28	$-1.128 \cdot 10^{-13} + [-1.779, 1.779]10^{-13}$
29	$5.294 \cdot 10^{-15} + [-5.796, 5.796]10^{-14}$
30	$-6.041 \cdot 10^{-14} + [-7.655, 7.655]10^{-14}$
31	$-2.807 \cdot 10^{-14} + [-3.384, 3.384]10^{-14}$
32	$-3.631 \cdot 10^{-15} + [-2.199, 2.199]10^{-14}$
33	$-7.325 \cdot 10^{-10} + [-3.017, 3.017]10^{-13}$
34	$2.608 \cdot 10^{-15} + [-4.228, 4.228]10^{-15}$
35	$-1.224 \cdot 10^{-16} + [-1.359, 1.359]10^{-15}$
36	$1.389 \cdot 10^{-15} + [-1.775, 1.775]10^{-15}$
37	$6.412 \cdot 10^{-16} + [-7.772, 7.772]10^{-16}$
38	$8.304 \cdot 10^{-17} + [-5.039, 5.039]10^{-16}$
39	$1.395 \cdot 10^{-11} + [-6.956, 6.956]10^{-15}$
40	$-5.841 \cdot 10^{-17} + [-9.691, 9.691]10^{-17}$
41	$2.718 \cdot 10^{-18} + [-3.085, 3.085]10^{-17}$
42	$-3.09 \cdot 10^{-17} + [-3.994, 3.994]10^{-17}$
43	$-1.421 \cdot 10^{-17} + [-1.738, 1.738]10^{-17}$
44	$-1.839 \cdot 10^{-18} + [-1.126, 1.126]10^{-17}$
45	$-2.655 \cdot 10^{-13} + [-1.557, 1.557]10^{-16}$
46 – 200	small intervals of width $\leq 10^{-17}$
$\geq 201$	$< 3.295 \cdot 10^{-44}/k^6$

The bounds above are within the set  $\mathcal{W}_s^{loc}$ , i.e., within the basin of attraction of the stable fixed point. This implies that the third step of the proof of the main theorem from Section 4 succeeded.

## A.2 Heteroclinic to the global minimizer

We present the analogous numerical data from the computer-assisted existence proof of the heteroclinic between the homogeneous state and the *global* minimizer.

**Unstable isolating block  $\mathcal{W}_u \subset H'$  around zero** This is the first step of the proof of the main theorem from Section 4). We mark with text in bold the numerical values for the eigendirection  $e_2$  along which the unstable manifold of the homogeneous state connects to the stable *global* minimizer

( $\mathcal{W}_u$  is stretched along this direction).

<b>k</b>	<b>a<sub>k</sub></b> interval in the form center + radius
1	$0 + [-1.105, 1.105]10^{-15}$
<b>2</b>	<b><math>[-0.1, 0.1]</math></b>
3	$0 + [-1, 1]10^{-12}$
4	$0 + [-7.235, 7.235]10^{-15}$
5	$0 + [-1.438, 1.438]10^{-15}$
6	$0 + [-6.918, 6.918]10^{-16}$
7	$0 + [-4.579, 4.579]10^{-16}$
8	$0 + [-2.626, 2.626]10^{-16}$
9	$0 + [-2.449, 2.449]10^{-16}$
10	$0 + [-1.742, 1.742]10^{-16}$
11	$0 + [-1.571, 1.571]10^{-16}$
12	$0 + [-1.054, 1.054]10^{-16}$
13	$0 + [-1.102, 1.102]10^{-16}$
14	$0 + [-8.963, 8.963]10^{-17}$
15	$0 + [-8.008, 8.008]10^{-17}$
16 – 75	small intervals of width $\leq 10^{-19}$
$\geq 76$	$< 6.925 \cdot 10^{-59}/k^6$

The infinite-dimensional cone condition (18) is satisfied with

$$\varepsilon = 0.2873.$$

The file *unstable\_box\_log.txt* which can be found online [13] contains more detailed numerical data related with this computation.

**Stable isolating block**  $\mathcal{W}_s^{glob} \subset H'$  (The second step of the proof of the main theorem from Section 4)  $\mathcal{W}_s^{glob}$  is centered at a numerically computed approximation to the actual global stable equilibrium loaded from the provided file *fixedPointGlobal.in*.

Observe that although the dimension of the finite-dimensional tail here is larger (300), the diameters of  $\mathcal{W}_s^{glob}$  are now considerably larger, as well as the  $\varepsilon$  cone condition value, than in the case of the local minimizer. This is due to the fact that the global minimizer is stronger attracting than the local minimizer in the sense that the maximal eigenvalue of the Jacobian matrix at the global minimizer is

further away from zero than the maximal eigenvalue at the local minimizer.

<b>k</b>	<b><math>\mathbf{a}_k</math></b>		
1	$-6.339 \cdot 10^{-18} + [-2.122, 2.122]10^{-5}$	25	$2.058 \cdot 10^{-18} + [-2.564, 2.564]10^{-7}$
<b>2</b>	<b><math>0.3484 + [-2.368, 2.368]10^{-5}</math></b>	26	$1.465 \cdot 10^{-8} + [-2.352, 2.352]10^{-7}$
3	$3.969 \cdot 10^{-17} + [-4.191, 4.191]10^{-5}$	27	$3.304 \cdot 10^{-19} + [-2.936, 2.936]10^{-7}$
4	$-1.125 \cdot 10^{-15} + [-1.129, 1.129]10^{-5}$	28	$-3.412 \cdot 10^{-17} + [-1.982, 1.982]10^{-7}$
5	$3.558 \cdot 10^{-17} + [-1.213, 1.213]10^{-5}$	29	$-2.625 \cdot 10^{-19} + [-1.998, 1.998]10^{-7}$
6	$-0.02108 + [-7.626, 7.626]10^{-6}$	30	$-8.656 \cdot 10^{-10} + [-1.384, 1.384]10^{-7}$
7	$-9.56 \cdot 10^{-18} + [-9.823, 9.823]10^{-6}$	31	$1.09 \cdot 10^{-19} + [-2.202, 2.202]10^{-7}$
8	$4.792 \cdot 10^{-16} + [-4.311, 4.311]10^{-6}$	32	$-1.348 \cdot 10^{-17} + [-2.093, 2.093]10^{-7}$
9	$-2.52 \cdot 10^{-18} + [-4.51, 4.51]10^{-6}$	33	$1.483 \cdot 10^{-19} + [-2.814, 2.814]10^{-7}$
10	$1.207 \cdot 10^{-3} + [-2.687, 2.687]10^{-6}$	34	$5.115 \cdot 10^{-11} + [-2.029, 2.029]10^{-7}$
11	$4.678 \cdot 10^{-18} + [-2.501, 2.501]10^{-6}$	35	$2.292 \cdot 10^{-19} + [-1.962, 1.962]10^{-7}$
12	$-1.251 \cdot 10^{-15} + [-1.19, 1.19]10^{-6}$	36	$-4.436 \cdot 10^{-17} + [-1.683, 1.683]10^{-7}$
13	$7.395 \cdot 10^{-18} + [-1.571, 1.571]10^{-6}$	37	$2.326 \cdot 10^{-19} + [-2.629, 2.629]10^{-7}$
14	$-7.109 \cdot 10^{-5} + [-1.238, 1.238]10^{-6}$	38	$-3.022 \cdot 10^{-12} + [-2.325, 2.325]10^{-7}$
15	$5.117 \cdot 10^{-18} + [-1.442, 1.442]10^{-6}$	39	$3.417 \cdot 10^{-20} + [-2.932, 2.932]10^{-7}$
16	$-4.127 \cdot 10^{-16} + [-9.132, 9.132]10^{-7}$	40	$-3.135 \cdot 10^{-12} + [-7.641, 7.641]10^{-10}$
17	$2.433 \cdot 10^{-18} + [-8.563, 8.563]10^{-7}$	41	$-4.553 \cdot 10^{-12} + [-1.109, 1.109]10^{-9}$
18	$4.197 \cdot 10^{-6} + [-4.648, 4.648]10^{-7}$	42	$-3.567 \cdot 10^{-12} + [-9.137, 9.137]10^{-10}$
19	$-1.265 \cdot 10^{-18} + [-6.274, 6.274]10^{-7}$	43	$-4.418 \cdot 10^{-12} + [-1.076, 1.076]10^{-9}$
20	$4.897 \cdot 10^{-17} + [-5.667, 5.667]10^{-7}$	44	$-1.845 \cdot 10^{-13} + [-7.486, 7.486]10^{-11}$
21	$-2.285 \cdot 10^{-19} + [-7.082, 7.082]10^{-7}$	45	$-3.045 \cdot 10^{-13} + [-1.092, 1.092]10^{-10}$
22	$-2.479 \cdot 10^{-7} + [-4.735, 4.735]10^{-7}$	46	$-2.93 \cdot 10^{-13} + [-9.065, 9.065]10^{-11}$
23	$1.889 \cdot 10^{-18} + [-4.624, 4.624]10^{-7}$	47	$-3.638 \cdot 10^{-13} + [-1.075, 1.075]10^{-10}$
24	$-2.62 \cdot 10^{-16} + [-2.606, 2.606]10^{-7}$	48 – 300	small intervals of width $10^{-12}$
		$\geq 301$	$< 5.334 \cdot 10^{-44}/k^6$

The infinite-dimensional cone condition (18) is satisfied with

$$\varepsilon = 0.7869,$$

which equivalently means that the logarithmic norm estimate is negative.

The file *stable\_box\_log.txt* that can be found online [13] contains more detailed numerical data related with this computation. As in the case of the local minimizer, the interval radii of the first 39 modes (separated above with a horizontal line) of  $\mathcal{W}_s^{glob}$  are given in the eigenbasis of the finite-dimensional derivative at  $z_0^{s, glob}$ .

**Result of the numerical integration** This is the third and final step of the proof of the main theorem from Section 4. Some technical parameters of the numerical integration are chosen in the following way:

- The Taylor method order is 16,
- the constant time step is 0.002,
- the Galerkin projection dimension  $m$  is 15, the dimension used by the FFT-algorithm  $N$  is 32, see also the description in Section 5.
- The whole integration process took **6m34s** on an Intel®Core™i7-4610M CPU @ 3.00GHz x 4, compiled with gcc version 4.9.2 (64-bit Ubuntu 4.9.2-10ubuntu13) and with flags -O2 -frounding-math.
- In contrast, if instead of the FFT-algorithm we used the direct algorithm, then the whole integration process took **17m29s**.

The file *num\_integration\_log.txt* that can be found online [13] contains more detailed numerical data related to this computation. Specifically, the file contains

- the vector which is the finite-dimensional part of the propagated polynomial bounds, saved at each step of the integration,
- each 100 steps of the integration the full infinite-dimensional polynomial bounds,
- at each step of the integration information at which coordinates the entry of  $\mathcal{W}_0$  into  $\mathcal{W}_s^{glob}$  has not yet been attained.

The infinite-dimensional bounds at time  $T = 4.62$  after performing 2310 numerical integration steps are

<b>k</b>	<b>a<sub>k</sub></b>
1	$-1.13 \cdot 10^{-7} + [-5.199, 5.199]10^{-8}$
<b>2</b>	<b>0.3484 + [-7.806, 7.806]10<sup>-9</sup></b>
3	$-3.735 \cdot 10^{-7} + [-5.197, 5.197]10^{-8}$
4	$2.276 \cdot 10^{-7} + [-2.347, 2.347]10^{-9}$
5	$4.499 \cdot 10^{-8} + [-1.555, 1.555]10^{-8}$
6	$-0.02108 + [-1.812, 1.812]10^{-9}$
7	$-1 \cdot 10^{-7} + [-7.195, 7.195]10^{-9}$
8	$-2.038 \cdot 10^{-8} + [-4.573, 4.573]10^{-10}$
9	$4.559 \cdot 10^{-8} + [-1.703, 1.703]10^{-9}$
10	$1.207 \cdot 10^{-3} + [-2.437, 2.437]10^{-10}$
11	$-1.722 \cdot 10^{-8} + [-7.148, 7.148]10^{-10}$
12	$-2.243 \cdot 10^{-8} + [-2.337, 2.337]10^{-10}$
13	$1.96 \cdot 10^{-8} + [-1.743, 1.743]10^{-10}$
14	$-7.098 \cdot 10^{-5} + [-6.009, 6.009]10^{-11}$
15	$-1.855 \cdot 10^{-10} + [-2.586, 2.586]10^{-10}$
16	$8.757 \cdot 10^{-11} + [-3.642, 3.642]10^{-10}$
17	$-9.373 \cdot 10^{-11} + [-3.223, 3.223]10^{-10}$
18	$4.195 \cdot 10^{-6} + [-1.181, 1.181]10^{-9}$
19	$-4.39 \cdot 10^{-12} + [-3.988, 3.988]10^{-11}$
20	$-1.142 \cdot 10^{-11} + [-3.233, 3.233]10^{-11}$
21	$1.051 \cdot 10^{-11} + [-2.777, 2.777]10^{-11}$
22	$-2.478 \cdot 10^{-7} + [-1.064, 1.064]10^{-10}$
23	$3.143 \cdot 10^{-13} + [-2.981, 2.981]10^{-12}$
24	$8.888 \cdot 10^{-13} + [-2.403, 2.403]10^{-12}$
25	$-8.013 \cdot 10^{-13} + [-2.045, 2.045]10^{-12}$
26	$1.464 \cdot 10^{-8} + [-7.9, 7.9]10^{-12}$
27	$-2.201 \cdot 10^{-14} + [-2.113, 2.113]10^{-13}$
28	$-6.322 \cdot 10^{-14} + [-1.699, 1.699]10^{-13}$
29	$5.65 \cdot 10^{-14} + [-1.436, 1.436]10^{-13}$
30	$-8.65 \cdot 10^{-10} + [-5.562, 5.562]10^{-13}$
31	$1.5 \cdot 10^{-15} + [-1.458, 1.458]10^{-14}$
32	$4.326 \cdot 10^{-15} + [-1.168, 1.168]10^{-14}$
33	$-3.846 \cdot 10^{-15} + [-9.814, 9.814]10^{-15}$
34	$5.111 \cdot 10^{-11} + [-3.809, 3.809]10^{-14}$
35	$-1.003 \cdot 10^{-16} + [-9.878, 9.878]10^{-16}$
36	$-2.894 \cdot 10^{-16} + [-7.888, 7.888]10^{-16}$
37	$2.563 \cdot 10^{-16} + [-6.592, 6.592]10^{-16}$
38	$-3.02 \cdot 10^{-12} + [-2.562, 2.562]10^{-15}$
39	$6.611 \cdot 10^{-18} + [-6.603, 6.603]10^{-17}$
40	$1.906 \cdot 10^{-17} + [-5.255, 5.255]10^{-17}$
41	$-1.684 \cdot 10^{-17} + [-4.373, 4.373]10^{-17}$
42	$1.785 \cdot 10^{-13} + [-1.702, 1.702]10^{-16}$
43	$-4.31 \cdot 10^{-19} + [-4.366, 4.366]10^{-18}$
44	$-1.241 \cdot 10^{-18} + [-3.464, 3.464]10^{-18}$
45	$1.094 \cdot 10^{-18} + [-2.872, 2.872]10^{-18}$
46	$-1.055 \cdot 10^{-14} + [-1.118, 1.118]10^{-17}$
47	$2.785 \cdot 10^{-20} + [-2.861, 2.861]10^{-19}$
48	$8.009 \cdot 10^{-20} + [-2.264, 2.264]10^{-19}$
49 – 250	small intervals of width $10^{-19}$
$\geq 251$	$< 3.96 \cdot 10^{-64}/k^6$

The bounds above are within  $\mathcal{W}_s^{glob}$ , i.e., the basin of attraction of the stable fixed point, which means that the third step of the proof of the main theorem from Section 4 succeeded.

## References

- [1] M. Bahiana and Y. Oono. Cell dynamical system approach to block copolymers. *Physical Review A*, 41:6763–6771, 1990.
- [2] F. A. Bartha and W. Tucker. Fixed points of a destabilized Kuramoto–Sivashinsky equation. *Applied Mathematics and Computation*, 266:339 – 349, 2015.
- [3] P. W. Bates and P. C. Fife. The dynamics of nucleation for the Cahn-Hilliard equation. *SIAM Journal on Applied Mathematics*, 53(4):990–1008, 1993.
- [4] D. Blömker, B. Gawron, and T. Wanner. Nucleation in the one-dimensional stochastic Cahn-Hilliard model. *Discrete and Continuous Dynamical Systems, Series A*, 27(1):25–52, 2010.
- [5] X. Cabré, E. Fontich, and R. de la Llave. T. parameterization method for invariant manifolds i: manifolds associated to non-resonant subspaces. *Indiana Univ. Math. J.*, 52:283–328, 2003.
- [6] J. W. Cahn and J. E. Hilliard. Free energy of a nonuniform system I. Interfacial free energy. *Journal of Chemical Physics*, 28:258–267, 1958.
- [7] R. Castelli, M. Gameiro, and J.-P. Lessard. Rigorous numerics for ill-posed PDEs: periodic orbits in the boussinesq equation. Preprint.

- [8] R. Choksi, M. Maras, and J. F. Williams. 2D phase diagram for minimizers of a Cahn-Hilliard functional with long-range interactions. *SIAM Journal on Applied Dynamical Systems*, 10(4):1344–1362, 2011.
- [9] R. Choksi, M. A. Peletier, and J. F. Williams. On the phase diagram for microphase separation of diblock copolymers: An approach via a nonlocal Cahn-Hilliard functional. *SIAM Journal on Applied Mathematics*, 69(6):1712–1738, 2009.
- [10] R. Choksi and X. Ren. On the derivation of a density functional theory for microphase separation of diblock copolymers. *Journal of Statistical Physics*, 113:151–76, 2003.
- [11] J. Cyranka. Efficient and generic algorithm for rigorous integration forward in time of dPDEs: Part I. *Journal of Scientific Computing*, 59(1):28–52, 2014.
- [12] J. Cyranka. Existence of globally attracting fixed points of viscous Burgers equation with constant forcing. a computer assisted proof. *Topological Methods in Nonlinear Analysis*, 45(2):655–697, 2015.
- [13] J. Cyranka. Numerical data and source codes from the proof. Technical report, 2017. [http://bitbucket.org/dzako/dbcp\\_proof](http://bitbucket.org/dzako/dbcp_proof).
- [14] J. Cyranka and P. Zgliczyński. Existence of globally attracting solutions for one-dimensional viscous Burgers equation with nonautonomous forcing—a computer assisted proof. *SIAM Journal on Applied Dynamical Systems*, 14(2):787–821, 2015.
- [15] A. Czechowski and P. Zgliczyński. Rigorous numerics for PDEs with indefinite tail: Existence of a periodic solution of the Boussinesq equation with time-dependent forcing. *Schedae Informaticae*, 2015(Volume 24), 2016.
- [16] G. Dahlquist. *Stability and Error Bounds in the Numerical Integration of Ordinary Differential Equations*. Transactions of the Royal Institute of Technology. Almqvist & Wiksells, Uppsala, 1958.
- [17] S. Day, Y. Hiraoka, K. Mischaikow, and T. Ogawa. Rigorous numerics for global dynamics: A study of the Swift–Hohenberg equation. *SIAM Journal on Applied Dynamical Systems*, 4(1):1–31, 2005.
- [18] J. P. Desi, H. Edrees, J. Price, E. Sander, and T. Wanner. The dynamics of nucleation in stochastic Cahn-Morral systems. *SIAM Journal on Applied Dynamical Systems*, 10(2):707–743, 2011.
- [19] P. C. Fife, H. Kielhöfer, S. Maier-Paape, and T. Wanner. Perturbation of doubly periodic solution branches with applications to the Cahn-Hilliard equation. *Physica D*, 100(3–4):257–278, 1997.
- [20] M. Gameiro, J.-P. Lessard, and A. Pugliese. Computation of smooth manifolds via rigorous multi-parameter continuation in infinite dimensions. *Found. Comput. Math.*, 16(2):531–575, 2016.
- [21] M. Grinfeld and A. Novick-Cohen. Counting stationary solutions of the Cahn-Hilliard equation by transversality arguments. *Proceedings of the Royal Society of Edinburgh*, 125A:351–370, 1995.
- [22] M. Grinfeld and A. Novick-Cohen. The viscous Cahn-Hilliard equation: Morse decomposition and structure of the global attractor. *Transactions of the American Mathematical Society*, 351(6):2375–2406, 1999.
- [23] J. D. M. James and K. Mischaikow. Rigorous a posteriori computation of (un)stable manifolds and connecting orbits for analytic maps. *SIAM Journal on Applied Dynamical Systems*, 12(2):957–1006, 2013.
- [24] I. Johnson, E. Sander, and T. Wanner. Branch interactions and long-term dynamics for the diblock copolymer model in one dimension. *Discrete and Continuous Dynamical Systems. Series A*, 33(8):3671–3705, 2013.
- [25] T. Kapela and P. Zgliczyński. A Lohner-type algorithm for control systems and ordinary differential inclusions. *Discrete and Continuous Dynamical Systems - Series B*, 11(2):365–385, 2009.
- [26] R. Lohner. *Computation of guaranteed enclosures for the solutions of ordinary initial and boundary value problems*, chapter Computational Ordinary Differential Equations. Clarendon Press, Oxford, 1992.
- [27] S. M. Lozinskii. Error estimates for the numerical integration of ordinary differential equations, part i. *Izv. Vyss. Uceb. Zaved. Matematika*, 6:52–90, 1958.
- [28] S. Maier-Paape, U. Miller, K. Mischaikow, and T. Wanner. Rigorous numerics for the Cahn-Hilliard equation on the unit square. *Revista Matemática Complutense*, 21(2):351–426, 2008.
- [29] S. Maier-Paape, K. Mischaikow, and T. Wanner. Structure of the attractor of the Cahn-Hilliard equation on a square. *International Journal of Bifurcation and Chaos*, 17(4):1221–1263, 2007.
- [30] S. Maier-Paape and T. Wanner. Solutions of nonlinear planar elliptic problems with triangle symmetry. *Journal of Differential Equations*, 136(1):1–34, 1997.
- [31] S. Maier-Paape and T. Wanner. Spinodal decomposition for the Cahn-Hilliard equation in higher dimensions. Part I: Probability and wavelength estimate. *Communications in Mathematical Physics*, 195(2):435–464, 1998.
- [32] S. Maier-Paape and T. Wanner. Spinodal decomposition for the Cahn-Hilliard equation in higher dimensions: Nonlinear dynamics. *Archive for Rational Mechanics and Analysis*, 151(3):187–219, 2000.
- [33] C. McCord. Mappings and homological properties in the Conley index theory. *Ergodic Theory and Dynamical Systems*, 8\*(Charles Conley Memorial Issue):175–198, 1988.

- [34] K. Mischaikow and M. Mrozek. *Conley Index*, volume 2 of *Handbook of Dynamical Systems*, chapter 9, pages 393–460. Elsevier, 2002.
- [35] R. Moore. *Interval Analysis*. Prentice Hall, Englewood Cliffs, N.J., 1966.
- [36] Z. Mączyńska. *Rigorous numerics for dissipative partial differential equations*. PhD thesis, Jagiellonian University, 2011, 2011.
- [37] Y. Nishiura and I. Ohnishi. Some mathematical aspects of the micro-phase separation in diblock copolymers. *Physica D*, 84(1-2):31–39, 1995.
- [38] T. Ohta and K. Kawasaki. Equilibrium morphology of block copolymer melts. *Macromolecules*, 19:2621–2632, 1986.
- [39] C. Reinhardt and J. Mireles James. Fourier-Taylor parameterization of unstable manifolds for parabolic partial differential equations: Formalism, implementation and rigorous validation. preprint arXiv:1601.00307v2, 2016.
- [40] X. Ren and J. Wei. On energy minimizers of the diblock copolymer problem. *Interfaces and Free Boundaries*, 5(2):193–238, 2003.
- [41] X. Ren and J. Wei. Droplet solutions in the diblock copolymer problem with skewed monomer composition. *Calculus of Variations and Partial Differential Equations*, 25(3):333–359, 2006.
- [42] X. Ren and J. Wei. Existence and stability of spherically layered solutions of the diblock copolymer equation. *SIAM Journal on Applied Mathematics*, 66(3):1080–1099, 2006.
- [43] X. Ren and J. Wei. Many droplet pattern in the cylindrical phase of diblock copolymer morphology. *Reviews in Mathematical Physics*, 19(8):879–921, 2007.
- [44] X. Ren and J. Wei. Single droplet pattern in the cylindrical phase of diblock copolymer morphology. *Journal of Nonlinear Science*, 17(5):471–503, 2007.
- [45] E. Sander and T. Wanner. Monte Carlo simulations for spinodal decomposition. *Journal of Statistical Physics*, 95(5–6):925–948, 1999.
- [46] E. Sander and T. Wanner. Unexpectedly linear behavior for the Cahn-Hilliard equation. *SIAM Journal on Applied Mathematics*, 60(6):2182–2202, 2000.
- [47] E. Sander and T. Wanner. Validated saddle-node bifurcations and applications to lattice dynamical systems. *SIAM Journal on Applied Dynamical Systems*, 15(3):1690–1733, 2016.
- [48] R. Temam. *Infinite-Dimensional Dynamical Systems in Mechanics and Physics*. Springer-Verlag, New York – Berlin – Heidelberg, 1988.
- [49] W. Tucker. *Validated numerics*. Princeton University Press, Princeton, NJ, 2011.
- [50] J. B. van den Berg, J. D. Mireles-James, J.-P. Lessard, and K. Mischaikow. Rigorous numerics for symmetric connecting orbits: Even homoclinics of the Gray–Scott equation. *SIAM Journal on Mathematical Analysis*, 43(4):1557–1594, 2011.
- [51] J. B. van den Berg, J. D. Mireles James, and C. Reinhardt. Computing (un)stable manifolds with validated error bounds: Non-resonant and resonant spectra. *Journal of Nonlinear Science*, 26(4):1055–1095, 2016.
- [52] J. B. van den Berg and J. Williams. Validation of the bifurcation diagram in the 2d ohta-kawasaki problem. preprint, 2016.
- [53] T. Wanner. Maximum norms of random sums and transient pattern formation. *Transactions of the American Mathematical Society*, 356(6):2251–2279, 2004.
- [54] T. Wanner. Computer-assisted bifurcation diagram validation and applications in materials science. *Submitted for publication*, 2016.
- [55] T. Wanner. Topological analysis of the diblock copolymer equation. In Y. Nishiura and M. Kotani, editors, *Mathematical Challenges in a New Phase of Materials Science*, volume 166 of *Springer Proceedings in Mathematics & Statistics*, pages 27–51. Springer-Verlag, 2016.
- [56] T. Wanner. Computer-assisted equilibrium validation for the diblock copolymer model. *Discrete and Continuous Dynamical Systems, Series A*, 37(2):1075–1107, 2017.
- [57] D. Wilczak. The existence of Shilnikov homoclinic orbits in the Michelson system: A computer assisted proof. *Foundations of Computational Mathematics*, 6(4):495–535, 2006.
- [58] D. Wilczak and P. Zgliczyński. Heteroclinic connections between periodic orbits in planar restricted circular three body problem. Part ii. *Communications in Mathematical Physics*, 259(3):561–576, 2005.
- [59] D. Wilczak and P. Zgliczyński. Topological method for symmetric periodic orbits for maps with a reversing symmetry. *Discrete and Continuous Dynamical Systems*, 17(3):629–652, 2007.
- [60] P. Zgliczynski. Attracting fixed points for the Kuramoto–Sivashinsky equation: A computer assisted proof. *SIAM Journal on Applied Dynamical Systems*, 1(2):215–235, 2002.

- [61] P. Zgliczynski. Rigorous numerics for dissipative partial differential equationsii. periodic orbit for the Kuramoto–Sivashinsky pde—a computer-assisted proof. *Foundations of Computational Mathematics*, 4(2):157–185, 2004.
- [62] P. Zgliczynski and K. Mischaikow. Rigorous numerics for partial differential equations: The Kuramoto—Sivashinsky equation. *Foundations of Computational Mathematics*, 1(3):255–288, 2001.
- [63] P. Zgliczyński. Covering relations, cone conditions and the stable manifold theorem. *Journal of Differential Equations*, 246(5):1774 – 1819, 2009.
- [64] P. Zgliczyński. Rigorous numerics for dissipative PDEs III. an effective algorithm for rigorous integration of dissipative PDEs. *Topological Methods in Nonlinear Analysis*, 36:197–262, 2010.
- [65] P. Zgliczyński. Heteroclinic connection in Kuramoto-Sivashinsky PDE - a computer assisted proof. preprint, 2016.
- [66] P. Zgliczyński and M. Gidea. Covering relations for multidimensional dynamical systems. *Journal of Differential Equations*, 202(1):32 – 58, 2004.
- [67] A. Ówieszewski and M. Maciejowski. Stationary solutions and connecting orbits for  $p$ -laplace equation. preprint, 2016.